BRNO UNIVERSITY OF TECHNOLOGY

Faculty of Chemistry

# MASTER'S THESIS

Brno, 2024 Dmitrii Golub


# BRNO UNIVERSITY OF TECHNOLOGY

VYSOKÉ UČENÍ TECHNICKÉ V BRNĚ

## FACULTY OF CHEMISTRY

FAKULTA CHEMICKÁ

## INSTITUTE OF MATERIALS SCIENCE

ÚSTAV CHEMIE MATERIÁLŮ


# EFFECT OF SUBSTRATE AND GEOMETRY ON THE SIZE OF THE ANOMALOUS NERNST PHENOMENON

VLIV SUBSTRÁTU A GEOMETRIE NA VELIKOST ANOMÁLNÍHO NERNSTOVA JEVU

MASTER'S THESIS

DIPLOMOVÁ PRÁCE


AUTHOR — Dmitrii Golub

AUTOR PRÁCE

SUPERVISOR — prof. RNDr. Vladimír Čech, Ph.D.

VEDOUCÍ PRÁCE



BRNO 2024

BRNO UNIVERSITY OF TECHNOLOGY
FACULTY OF CHEMISTRY

# Assignment Master's Thesis

| | | |
|---|---|---|
| Project no.: | FCH-DIP1914/2023 | Academic year: 2023/24 |
| Department: | Institute of Materials Science | |
| Student: | **Dmitrii Golub** | |
| Study programme: | Chemistry and Technology of Materials | |
| Field of study: | no specialisation | |
| Head of thesis: | **prof. RNDr. Vladimír Čech, Ph.D.** | |

## Title of Master's Thesis:

Effect of substrate and geometry on the size of the anomalous Nernst phenomenon

## Master's Thesis:

– Literature overview – compare various experimental techniques to determine the anomalous Nernst coefficient, thermal gradient evaluation, thermal conductivity of various substrates and overview of the measured anomalous Nernst coefficients in various materials.
– Training in advanced nanolithography – electron lithography, etching devices, magnetron sputtering
– Fabrication of devices for measuring the anomalous Nernst effect using different substrate materials and thin films
– Measurement of the anomalous Nernst effect using various techniques and analysis of the results

## Deadline for Master's Thesis delivery: 29.4.2024:

Master's Thesis should be submitted to the institute's secretariat in a number of copies as set by the dean This specification is part of Master's Thesis

| | | |
|---|---|---|
| Dmitrii Golub<br>student | prof. RNDr. Vladimír Čech, Ph.D.<br>Head of thesis | doc. Ing. František Šoukal, Ph.D.<br>Head of department |

In Brno dated 1.2.2024

prof. Ing. Michal Veselý, CSc.
Dean

# Abstrakt

Anomální Nernstův jev (ANE) je vznik příčného napětí v magnetických materiálech při aplikovaném podélném teplotním gradientu. Tento jev nachází potenciální aplikaci v oblasti spinové kaloritroniky a konverze tepelné energie. V této práci je zkoumán vliv substrátu vzorku a experimentální geometrie na anomální Nernstův jev ve vzorcích tenkých filmů permaloye naprašených na různých substrátech. Studium anomálního Nernstova jevu bylo provedeno na vzorcích na čtyřech různých substrátech s podstatně odlišnou tepelnou vodivostí. Kromě toho byly testovány čtyři různé techniky generování teplotního gradientu ve vzorcích: tři metody pro generování gradientu v rovině vzorku a jedna metoda pro generování gradientu mimo rovinu vzorku. Bylo pozorováno, že tepelná vodivost substrátu významně ovlivňuje velikost teplotního gradientu. V dvou konfiguracích v rovině byl naměřen konzistentní koeficient anomálního Nernstova jevu, gradient teploty mimo rovinu vzorku byl odhadnut na základě získaných dat.

Pro porovnání výsledků měření ANE byl použit permalloy – feromagnetická slitina složení $Ni_{77}Fe_{14}Cu_5Mo_4$. Permalloy byl aplikován na 4 různé substráty ($Al_2O_3$ (0001), Si (100), $SrTiO_3$ (100), MgO(100)) metodou magnetronového naprašování. Metodou UV litografie byly vyrobené vzorky pro měření ANE, pro měření teplotního gradientu na vzorcích také byly naprašené platinové teploměry, konfigurace vzorků použitých pro porovnání vlivu substrátu je ukázána ve Figure 14 a Figure 15. Tloušťka vrstvy permalloye činila 55-65 nm, což bylo určeno pomocí profilometru Dektak XT. Vrstva měla vysoce polykrystalickou až amorfní strukturu, což bylo zjištěno pomocí metody difrakce rentgenového záření. Magnetizace vzorku byla změřena metodou SQUID magnetometrie, směr v rovině vzorku je magneticky měkký, směr mimo rovinu vzorku je magneticky tvrdý, hodnota saturačního pole činí 0.1 T a 0.35 T resp. Platinové teploměry na vzorku byly kalibrované pomocí teploměru typu PT100 se známou funkcí závislosti odporu na teplotě.

Měření probíhalo ve kryostatu Oxford Instruments INTEGRA (Figure 23) s supravodivým magnetem a vložkou s variabilní teplotou. Před měřením každý vzorek byl stabilizován na teplotě 100 K. Platinový teploměr typu PT1000 byl využit jako ohřívač, proud přes teploměr byl určen pomocí skriptu tak, aby výkon teploměru činil přibližně 600 mW. Během měření hodnota magnetického pole se měnila krokem 0.02 T od 0.6 T do -0.6 T a zpět pro měření případné hysterezní smyčky, napětí na příčném kontaktu bylo měřeno při každé hodnotě magnetického pole.

Hodnoty příčného napětí byly antisymetrizovány (viz 3.3.2) a porovnány mezi sebou. Nejmenší hodnota ANE signálu (0.18 μV/K) byla naměřena na vzorku na Si (100) substrátu, největší hodnota činila 0.29 μV/K a byla naměřena na $SrTiO_3$ substrátu. Tepelná vodivost substrátu má významný vliv na hodnotu generovaného teplotního gradientu. Lineární charakter teplotního gradientu ve vzorku byl potvrzen pomocí COMSOL simulace.

Měření Nernstova jevu při různých hodnotách teplotního gradientu bylo provedeno na vzorku permalloye na $SrTiO_3$ substrátu. Naměřené hodnoty koeficientu ANE činily 0.29 μV/K při velikosti teplotního gradientu 13.200 K/mm a 0.22 μV/K při velikosti

teplotního gradientu 10.227 K/mm, rozdíl v teplotním gradientu byl určen změnou výkonu ohřívače. Rozdíl v naměřené velikosti koeficientu ANE může být považován za chybu měření.

Tři různé konfigurace pro měření ANE koeficientu ve směru roviny vzorku byly testovány. Konfigurace s externím ohřívačem (Figure 14) a integrovaným ohřívačem (Figure 17) vykazují konzistentní výsledky (0.16 a 0.25 μV/K resp.). Rozdíl mezi výsledky je způsoben různou teplotou měření (142 K a 177 K resp.).


# Abstract

The anomalous Nernst effect refers to the transverse voltage generated in magnetic materials to applied longitudinal temperature gradient. The effect holds promise for applications in spin caloritronics and enhanced thermoelectric energy conversion. Here, we investigate the influence of the sample substrate and experimental geometry on the anomalous Nernst effect in sputtered permalloy thin film samples. We investigated the anomalous Nernst effect on samples with four different substrates of substantially different thermal conductivities. Moreover, four distinct techniques of generating thermal gradient in our samples were tested: three methods for generating in-plane gradients and one method for the out-of-plane gradient generation. We observe that the substrate thermal conductivity significantly affects the magnitude of the temperature gradient. Consistent anomalous Nernst effect coefficient is measured in two in-plane configurations, out-of-plane temperature gradient was estimated based on the acquired data.



# Keywords

Altermagnetism, Nernst effect, thin films

# Klíčová slova

Altermagnetismus, Nernstův jev, tenké vrstvy

GOLUB, Dmitrii. *Vliv substrátu a geometrie na velikost anomálního Nernstova jevu.* Brno, 2024. Dostupné také z: https://www.vut.cz/studenti/zav-prace/detail/156256. Diplomová práce. Vysoké učení technické v Brně, Fakulta chemická, Ústav chemie materiálů. Vedoucí práce Vladimír Čech.

# DECLARATION

I declare that the diploma thesis has been worked out by myself and that all the quotations from the used literary sources are accurate and complete. The content of the diploma thesis is the property of the Faculty of Chemistry of Brno University of Technology and all commercial uses are allowed only if approved by both the supervisor and the dean of the Faculty of Chemistry, BUT.

.....

student's signature

# Acknowledgments

I would like to thank all the personnel of the Department of Spintronics and Nanoelectronics of the Institute of Physics of the Czech Academy of Sciences for their hospitality and guidance. I am particularly grateful to my advisor – Antonín Baďura, who made an inestimable contribution to this work through his support and constant feedback.

# Table of contents

# 1 Introduction

Spintronics introduces the spin degree of freedom into conventional electronics, aiming to enhance future devices and reduce energy consumption. In the related field of spincaloritronics, researchers examine the interactions between spin and heat. This field is driven not only by fundamental research interests but also by the potential to harvest and utilize waste heat from electronic devices, motivating the search for more efficient spincaloritronic materials.

One of the key phenomena in spincaloritronics is the Nernst effect, which stands for the generation of a transverse thermoelectric voltage, allowing the direct conversion of a temperature gradient into electrical voltage. In magnetically ordered materials, this effect becomes pronounced in a magnetic field and is known as the anomalous Nernst effect (ANE). Remarkably, in the last two decades, it has been shown that ANE does not necessarily scale with net magnetization; significant anomalous Nernst coefficients have also been identified in materials with negligible magnetization, arising from their intrinsic electronic properties. The pursuit of more efficient anomalous Nernst coefficients underscores the importance of establishing reliable procedures to quantify the coefficient.

The largest source of error typically arises from the experimental challenge of quantifying the thermal gradient, particularly in thin films. Unlike standard magneto-transport, where the current is confined to the conductive film, in magneto-thermal transport, the thermal gradient also impacts the substrate. This can complicate measurements, especially in thin films, where the substrate might influence the thermoelectric signal by anisotropic heat conductivity, by altering grain size, inducing strain and stress, or changing the interface of the thin film. The measurement technique and device geometry can also significantly affect the results, as the thin film geometry allows the use of various configurations to measure ANE. Moreover, the thermal gradient can be also generated locally by laser.

At the same time, measurements of the anomalous Nernst effect in thin films are crucial due to their prevalence in integrated circuit technology, the predominant method for fabricating electronic devices. Therefore, it is essential to develop reliable techniques to measure and accurately quantify the anomalous Nernst coefficient.

In this work, we first introduce the theoretical background related to the interactions of spin, electrons, and heat in solid materials and summarize the measured magnitudes of the anomalous Nernst coefficient in various compounds. We then describe the methods for generating and measuring the thermal gradient. In the experimental section, we prepare several identical devices on various substrates to compare the resulting thermal gradients and anomalous Nernst effect coefficients. We also evaluate different techniques for generating the thermal gradient and discuss the results in the context of thermal gradient homogeneity.

In the final section, we present an example of the anomalous Nernst effect measured in an emerging magnetic material – the altermagnetic thin film $Mn_5Si_3$. Precise quantification of the thermal gradient is crucial to contextualize the measured values with those existing in literature.

# 2 Theoretical part

## 2.1 Electronic and magnetic properties of solids

This chapter describes the fundamental physical concepts of electronic structure in solids, which is at the origin of the phenomenon of magnetism in its different forms.

### 2.1.1 Band structure of solids

The basic concept for describing electronic states in the condensed-matter system is the problem of the periodic Coulomb potential in a crystal lattice. This problem was simplified and solved for the one-dimensional crystal lattice by Felix Bloch (1)

Bloch solved the Schrodinger equation for an electron in a crystal lattice. Solutions of the equation can be described as plane waves modulated by periodic functions. Mathematically, the electron wave functions $\psi$ are written as:

$$\psi(r) = e^{ik \cdot r} \cdot u(r) \tag{2.1}$$

where $r$ is the position, $u$ is a periodic function that has the same period as a crystal lattice, $k$ is the wave vector which can be restricted to the first Brillouin zone..

For every value of $k$, there are multiple solutions for each $n$, and so the states of the electrons are split into several bands, each with $n$ index. $n$ here is called the *band state index*.

Functions of this form define the wave functions and the states of the electrons in crystalline solid materials. Bloch functions are the basis for the concept of the electronic band structure.

There are values of energy for which no Bloch function solutions of the Schrödinger equation exist. These energies form continuous regions, so-called forbidden bands, where $k$ has complex values. The width of the forbidden bands also called the band gap, defines the electronic properties of the material. There are three general types of materials defined by their band gap: metals, semiconductors, and insulators.

In the insulators, the band gap width is usually more than 5 eV and there are almost no electrons in the next allowed region after the band gap. The width of the band gap in the semiconductors is about 1 eV. Here, highest ocuppied band at zero temperature is called the valence band and the band with the higher energy is called the conduction band. Electrons can be excited from the valence band to the conduction band by increasing the temperature or applying the external voltage. In metals, the valence and the conduction bands overlap and the band gap between them does not exist. Furthermore, the electric properties are influenced by the position of the Fermi level with respect to the material's bands which corresponds to an energy level which has 50% probability of being occupied in thermodynamic equlibrium.

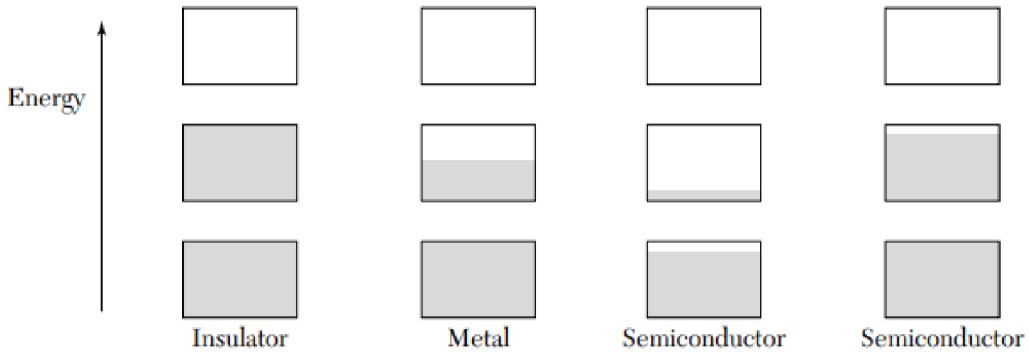


*Figure 1: The schematic structure of allowed energy bands for insulators, metals, and semiconductors. The vertical extent of the boxes indicates the allowed energy regions, and the grey areas indicate the regions filled with electrons. The left panel of a semiconductor corresponds to finite temperature with thermally excited carriers. The right panel semiconductor is electron-deficient because of impurities in the crystal. Adopted from (72)*

### 2.1.2 Magnetic order in solids

The fundamental object in magnetism is a dipole magnetic moment. According to classical electromagnetism, we can equate this with an infinitely small current loop, then the relationship between the magnetic moment and the current density $j$ can be formulated as follows:

$$m = \frac{1}{2}\int r \times j(r)\, d^3r, \tag{2.2}$$

where $r$ is the radius vector.

In solid materials, magnetization $M$ can be introduced as a local average of the magnetic moments in a mesoscopic volume $\delta V$:

$$\delta m = M(r)\delta V \tag{2.3}$$

Magnetic moment and magnetization are axial vectors, which means that they change sign under the time-reversal $t \to -t$ change, but remain unchanged under the spatial inversion $r \to -r$, in contrast to the standard polar vectors, such as position in space or current density, that change sign for both inversions *(2)*.

In a solid material, the magnetic field $B$ is related to the field intensity $H$ and magnetization $M$ through the formula:

$$B = \mu_0(H + M) = \mu_0(1 + \chi)H = \mu H, \tag{2.4}$$

where $\chi$ is a dimensionless quantity called the magnetic susceptibility and $\mu$ is magnetic permeability. Both of these variables are material-dependent tensors, and $\chi$ plays an important role when describing magnetically ordered materials. (69)

Magnetic moments in a crystal lattice can be organized in a variety of ways. In this chapter, we will describe four textbook types of magnetic order: diamagnetism,

paramagnetism, ferromagnetism, and antiferromagnetism, as well as the recently proposed concept of altermagnetism.

The magnetic moment of an electron in an atom is composed of two components. Firstly, there is the contribution due to the electron orbital angular momentum, which is equivalent to a classical picture of a magnetic moment generated by the orbital motion of an electron around a nucleus via Ampère's circuital law. The second contribution has no classical counterpart and corresponds to the electron spin, its inherent degree of freedom.

The electrons in a material are arranged in orbitals, which can be classically considered to be current loops with zero resistance. Any externally applied magnetic field will induce the opposite magnetic field in that loop. This effect is called diamagnetism and results in a negative contribution to magnetic susceptibility. Diamagnetic materials are therefore *weakly repelled* by the external magnetic field. Diamagnetism can occur in any material, but it can be overcome by other effects.

If the number of electrons in an atom shell is odd, the external magnetic field can cause the unpaired electrons to align their spins parallel to the external magnetic field, causing a net attraction. This type of magnetic order is called paramagnetism and results in a positive contribution to susceptibility. The number of aligned spins increases linearly depending on the strength of the magnetic field. In the absence of the external magnetic field, spins will be randomized due to thermal motion. Paramagnetic materials are *weakly attracted* by the external magnetic field.

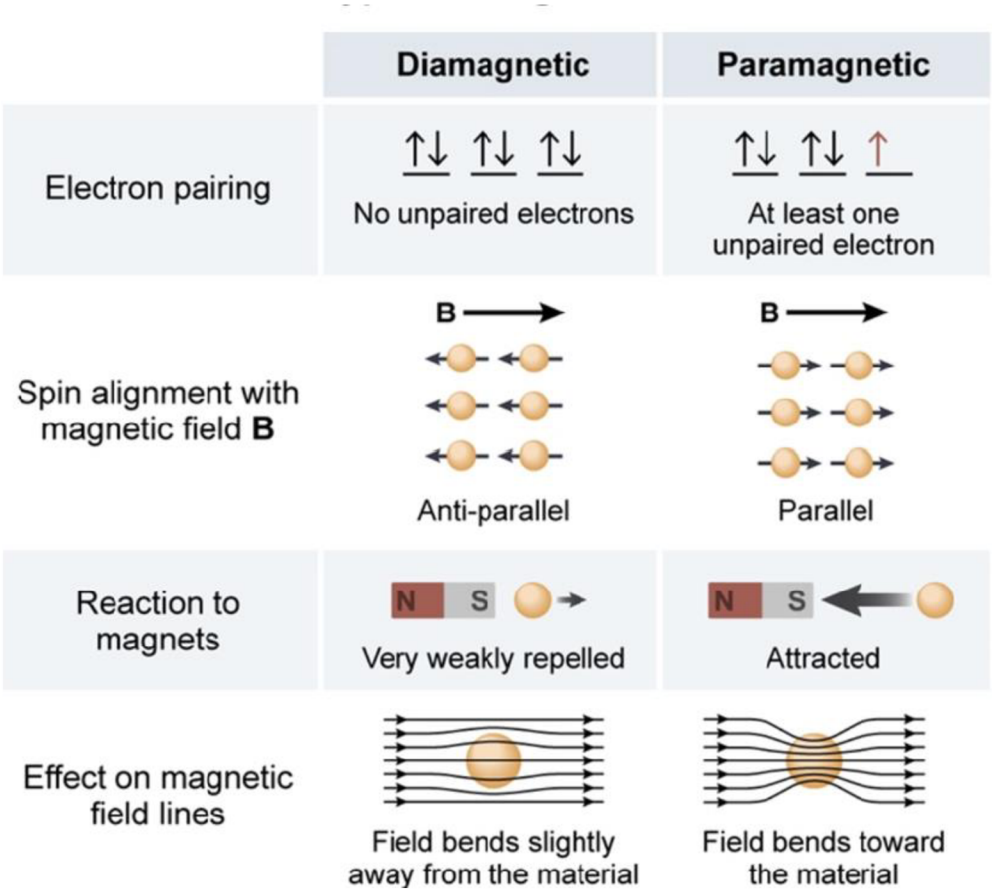


*Figure 2: Illustration of the differences between diamagnetic and paramagnetic materials. Adopted from (3)*

When two closely localized atoms have unpaired electrons, their spin orientation (parallel or antiparallel) can affect whether those electrons can occupy the same orbital due to the *exchange interaction.* The exchange interaction is the consequence of the Coulomb interaction presence and the Pauli exclusion principle and causes that electrons may prefer to align their spins parallel or antiparallel depending on their particular wavefunctions. The energy difference between the parallel and antiparallel configuration of the spins is called *exchange energy* and is described by the exchange integral $\bar{J}_{i,j}$:

$$H = -\sum_{i,j} \bar{J}_{i,j} \hat{s}_i \cdot \hat{s}_j \qquad (2.5)$$

where $\hat{s}_{i,j}$ are operators describing the electrons' spin.

Values of the exchange energy can be (up to $10^3$ for Fe) bigger than the energy of the dipole-dipole interactions in the paramagnetics. Exchange interaction causes ferromagnetic, antiferromagnetic, and ferrimagnetic orderings.

Ferromagnets demonstrate spontaneous magnetization even in the absence of an external magnetic field. The exchange integral of ferromagnets is positive, and so all the magnetic moments lie along a single direction due to the exchange interaction. The parallel ordering collapses at the Curie temperature, where the thermal fluctuations overcome the exchange energy, and the material becomes paramagnetic. The orientation of the magnetization in

a ferromagnet is determined by the effect of magnetocrystalline anisotropy, which makes certain crystallographic directions more favorable for magnetization to align along.

The ferromagnetic materials usually do not exist in a state with the same magnetization throughout the material, but in a state consisting of spontaneously oriented ferromagnetic domains. The reason for that is minimizing the internal (magnetostatic) energy of the material. Any large region of ferromagnetic material with constant magnetization throughout will create a large magnetic field extending into the space outside itself. This requires a lot of magnetostatic energy stored in the field. To reduce this energy material splits into loop-oriented domains, so that the magnetic field lines are looped inside of the material.

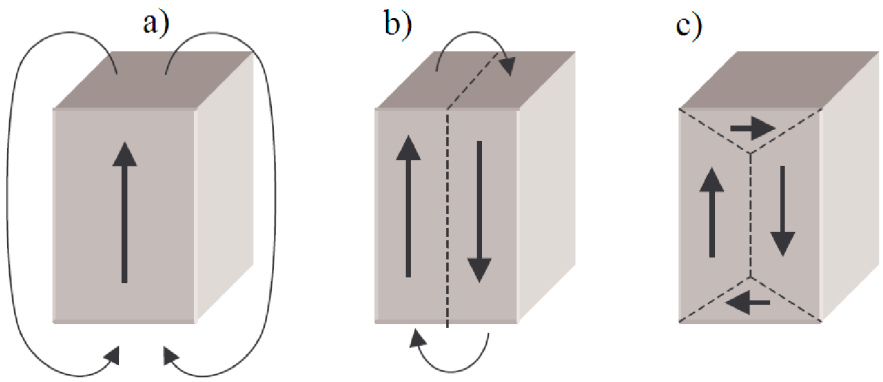


*Figure 3: Illustration of ferromagnetic material splitting into magnetic domains. (4)*

Antiferromagnets have a negative integral of the exchange interaction. Therefore, the magnetic moments aim to be aligned antiparallel, resulting in zero net magnetization. In the *collinear antiferromagnets,* there are two ferromagnetic spin-sublattices with the opposite orientation of magnetization. The magnetic ordering persists until the Neél temperature when the material usually becomes paramagnetic due to thermal fluctuations. However, the magnetic order in antiferromagnets can be more complicated when the magnetic moments are not parallel. This effect is called non-collinear antiferromagnetism. An example of such behavior is demonstrated on a triangular crystal lattice in Figure 4.

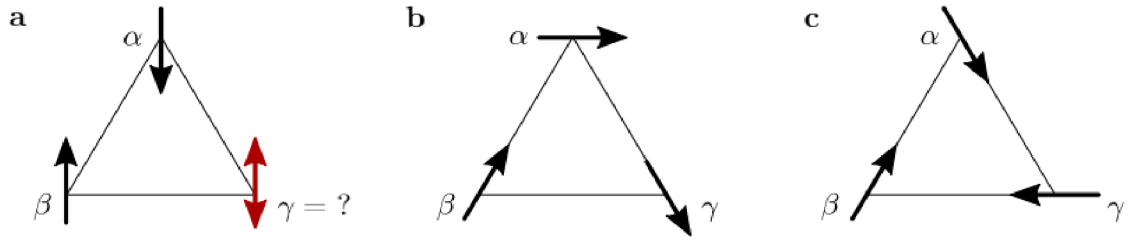


*Figure 4: Illustration of frustrated magnetic moments within a triangular lattice. γ moment is frustrated due to competing exchange interactions with α and β. Illustrations b and c show possible lowest energy configurations resulting in non-collinear ordering. (69)*

That frustration in non-collinear antiferromagnets is usually removed by antisymmetric exchange interaction or magnetocrystalline anisotropy, which results in a stable noncollinear magnetic order (5) (6) (7). The frustration of magnetic moments can also lead to more complex configurations, where spins are not ordered in one plane, such magnetic structures are called noncoplanar. (69)

While the band structure of paramagnetic and antiferromagnetic material shows the same energy value for spin-up and spin-down states, energy values in ferromagnetic materials for those states are different (Figure 5)

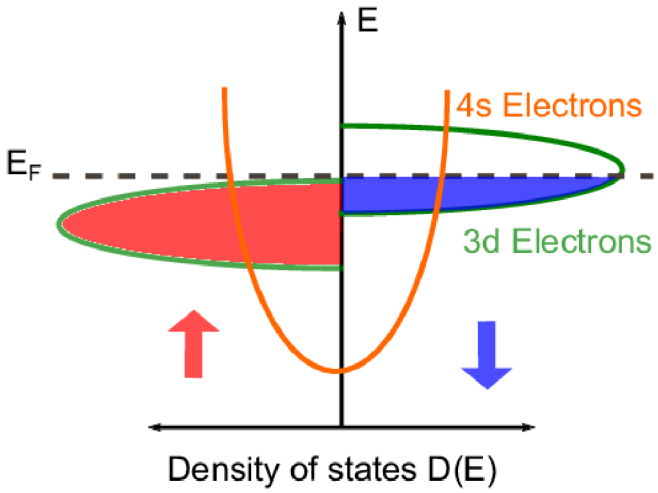


*Figure 5: A simplified band structure of a ferromagnetic metal showing the splitting of the 3d band and net density of states at the Fermi level between spin-up and spin-down states. Arrows indicate the spin direction of the carriers. (8)*

We have described some types of magnetic order in solid materials based on the mutual arrangement of local magnetic moments in real space. However, the modern and more precise strategy is characterization of magnetic order using reciprocal space and electronic band structure (9). That change of approach was motivated by theoretical predictions of time-symmetry breaking macroscopic phenomena and spin-split band structures (which are typical for ferromagnetic ordering) appearing in crystals with

compensated antiparallel magnetic ordering, which is characteristic of antiferromagnets. Recent symmetry classification and description (10) uses a generalized symmetry formalism to describe the spin arrangement on crystals, allowing to describe a broad landscape of magnetic phases by considering symmetry transformations that combine generally different operations in real and spin space. The new classification based on this symmetry formalism establishes a third distinct and comparably abundant phase. That phase is characterized by compensated magnetic order in direct space with opposite-spin sublattices connected by crystal-rotation symmetries, and by a corresponding unconventional spin-polarization order in the reciprocal space that reflects the same rotation symmetries. That correspondence of direct and reciprocal space symmetries results in an electronic band structure with broken time-reversal symmetry and alternating momentum-dependent sign of spin splitting. Šmejkal et al. introduced a new name *altermagnets* (10) to distinguish that phase from convenient ferromagnets and antiferromagnets. The difference between the band structure of altermagnets, ferromagnets, and antiferromagnets is illustrated in Figure 6.

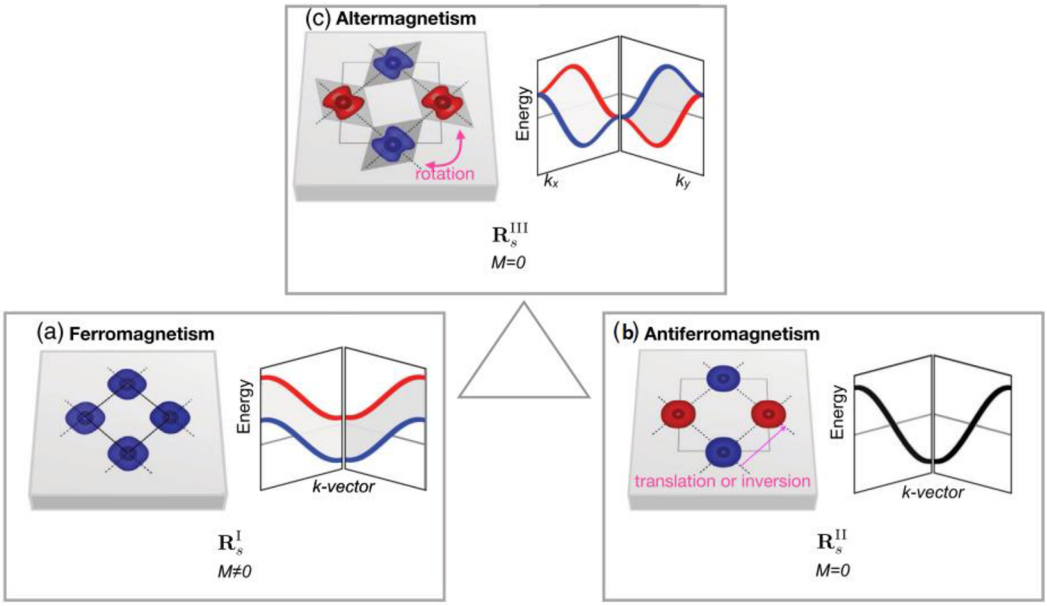


*Figure 6: Illustration of ferromagnetic, antiferromagnetic, and altermagnetic phases in real space and nonrelativistic electronic-structure momentum space. Adopted from (11)*

The altermagnetic spin-splitting originates from a local anisotropic electric field *(12)*, such mechanism contrasts with the conventional ferromagnetic splitting due to the exchange interaction or the spin-orbit splitting. The spin-splitting can induce various magnetism-related phenomena, such as anomalous Hall and anomalous Nernst effects. The list of rules for identifying altermagnets and a detailed list of candidate altermagnetic materials, including $MnO_2$, $RuO_2$, $La_2CuO_4$, and $Mn_5Si_3$ was provided by Šmejkal et al. *(10)*.

## 2.2 Theory of charge and heat transport in solids

### 2.2.1 Drude model

Drude (13) proposed his theory of conductivity to explain the transport properties of electron in materials (especially metals). The Drude model attempts to explain the conductivity in terms of kinetic theory, i.e. scattering of the electrons on the immobile positively charged ions, which obstruct the flow of the free electron gas.

Basic assumptions of Drude's theory:

1. The number density of the electron gas is assumed to be:

$$n = \frac{N_A Z \rho_m}{A}, \tag{2.6}$$

where $Z$ is the effective number of de-localized electrons per ion, for which Drude used the valence number, $A$ is the atomic mass per mole, $\rho_m$ is the mass density (mass per unit volume) of the ions, and $N_A$ is the Avogadro constant.

2. Interactions of ions and electrons between collisions are neglected.
3. Collisions are instantaneous events that abruptly alter the velocity of the electron.
4. There is a probability of collision per unit of time $1/\tau$. The time $\tau$ is known as a relaxation time and plays a fundamental role in the theory of metallic conduction.
5. Electrons can achieve thermal equilibrium with their surroundings only through collisions.

The Drude model provides an estimate size of the size of the electrical conductivity, which can be considered a quantitative value of the material.

According to Ohm's law, the current flow $I$ is directly proportional to the potential drop $V$ along the conductor and inversely proportional to the resistivity $R$. $R$ here depends on the size of the conductor and intrinsic properties of the material. That intrinsic resistivity $\rho$ is defined to be proportionally constant between the electric field $E$ and the current density j that it induces.

$$E = \rho j \tag{2.7}$$

Here, $j$ is a vector, parallel to the flow of charge, which magnitude is the amount of charge crossing a unit area perpendicular to the flow.

If $n$ electrons with the elementary charge e are moving with average velocity $v$, the current density can be written as:

$$J = -nev \tag{2.8}$$

In the presence of the external field E, the average speed can be computed in terms of the relaxation time.

$$v_{avg} = \frac{-eE\tau}{m} \tag{2.9}$$

And so the expression for $j$ is:

$$j = \frac{ne^2\tau}{m}E = \sigma E \qquad (2.10)$$

The relaxation time can now be computed using the observed resistivity of the materials, typical relaxation time at room temperature is of order $10^{-14}$ s.

### 2.2.2 Transport equations

The relaxation-time approximation overlooks the fact that electron scattering also depends on the nonequilibrium electronic distribution function, which will differ in different experimental situations. One can use a more accurate description of the collisions considering the impurities and defects of the crystal and the deviations from periodicity in a crystal due to thermal vibrations of the ions.

A more realistic description of the collisions assumes the probability per time unit that an electron in the n band with wave vector k will be scattered into the n‘ band with another wave vector k‘. The scattering probability can be written in terms of quantity $w_{k,k'}$. The probability in a time interval $dt$ that an electron with wave vector $k$ is scattered into any of the group of levels inside the k-space element $dk'$ about $k'$ considering those levels fully occupied and thus non-forbidden by the exclusion principle can be written as:

$$\frac{w_{k,k}\, dt\, dk'}{(2\pi)^3} \qquad (2.11)$$

The probability function depends on the particular scattering mechanism being described, but it will generally have quite complex structure, which also depends on the electronic distribution function *f*.

The total probability of collision per time unit is given by summing over all final wave vectors $k'$**:**

$$\frac{1}{\tau(k)} = \int \frac{dk\prime}{(2\pi)^3} W_{k,k\prime}[1-f(k')] \qquad (2.12)$$

$\tau(k)$ here, in contrast to the relaxation time approximation is not a specified function of $k$, but depends on the particular form of the nonequilibrium distribution function *f*.

Three types of effects affect the dynamic behavior of the distribution function $f$:

1. Carriers can move in and out of the region r. If $v_k$is the velocity of a carrier in the $k$ state, then there is an interval t, during which the carriers in this state will travel a distance $tv_K$. So, the number of carriers in region r at time t is equal to the number of them in the region $r - tv_k$ at time 0:

   $$f(r,t) = f(r - tv_k, 0) \qquad (2.13)$$

   So the rate of change in the distribution f due to the diffusion effect is:

   $$\frac{\partial f_k}{\partial t}\Big]\, diff. = -v_k \cdot \frac{\partial f_k}{\partial r} = -v_k \cdot \nabla f_k \qquad (2.14)$$

2. External fields will change the k-vector of each carrier:

$$k = \frac{e}{\hbar}\left(E + \frac{1}{c} v_k \wedge B\right) \tag{2.15}$$

And so, the distribution will change at the rate

$$\frac{\partial f_k}{\partial t}\Big] field = -k \cdot \frac{\partial f_k}{\partial k} = \frac{-e}{\hbar}\left(E + \frac{1}{c} v_k \wedge B\right) \cdot \frac{\partial f_k}{\partial k} \tag{2.16}$$

3. Although the scattering effect is complicated, we can consider it elastic. The change of the distribution will be written as:

$$\frac{\partial f_k}{\partial t}\Big] scatt. = \int \{f_{k'}(1 - f) - f_k(1 - f_{k'})\}\, Q(k, k') dk' \tag{2.17}$$

Scattering from $k$ to $k'$ decreases $f_k$, the probability of this process depends on $f_k$, the number of carriers in the $k$ state, and on $(1 - f_k)$, the number of vacancies available in the final state. The inverse process from $k'$ to $k$is weighted with $f_k(1 - f_k)$.

The Boltzmann equation says that at any point and for any $k$, the net rate of change of $f_k r$ is zero and so:

$$\frac{\partial f_k}{\partial t}\Big] scatt. + \frac{\partial f_k}{\partial t}\Big] field + \frac{\partial f_k}{\partial t}\Big] diff. = 0 \tag{2.18}$$

This is the steady state, not the actual equilibrium state $f_k^0$ (which holds when fields and temperature gradients are absent), but we can assume that the steady-state distribution does not depart very far from the equilibrium:

$$g_k = f_k - f_k^0 \tag{2.19}$$

Where $f_k^0$is:

$$f_k^0 = \frac{1}{exp\left\{\frac{\varepsilon_k - \zeta}{kT}\right\} + 1} = f^0(\varepsilon_k) \tag{2.20}$$

$\zeta$ here is chemical potential which is equal to Fermi level $\varepsilon_F$ at $T = 0$

If we suppose that we have an electric field as well as a temperature gradient in the specimen the Boltzmann equation is:

$$\frac{-\partial f^0}{\partial \varepsilon} v_k \cdot \left\{\frac{\varepsilon(k) - \zeta}{T}(-\nabla T) + e\left(E - \frac{1}{e}\nabla\zeta\right)\right\} = \frac{-\partial f_k}{\partial t}\Big] scatt. \tag{2.21}$$

The $k$ vector function describes the influence of temperature gradient $\nabla T$ and electric field $E$. The solution for this equation in the relaxation time approximation is:

$$f_k - f_k^0 = \left(\frac{-\partial f^0}{\partial \varepsilon}\right) \tau v_k \cdot \left[e\left(E - \frac{1}{e}\nabla\zeta\right) + \frac{\varepsilon(k) - \zeta}{T}(-\nabla T)\right] \tag{2.22}$$

Using that form of the Boltzmann equation we can now finally construct the general transport equations for the electric current $J_e$ and the flux of heat $J_q$:

$$J_e = \overline{\sigma} \cdot E - \overline{\alpha}\nabla T \tag{2.23}$$

$$J_q = T\overline{\alpha}E - \overline{\kappa}\nabla T \tag{2.24}$$

$\overline{\sigma}$ here is the electric conductivity tensor, $\overline{\kappa}$ is the thermal conductivity tensor and $\overline{\alpha}$ is the thermoelectric tensor. Each diagonal and off-diagonal component of these tensors is set by one of the six independent Onsager coefficients.

Nernst coefficient $S_{xy}$ can now be defined as off-diagonal component of the $S$ tensor:

$$E = \rho \cdot J_e - S\nabla T \tag{2.25}$$

### 2.2.3 Hall effect, Nernst effect, Mott relation

The described charge transport mechanism is a theoretical basis for studying various properties of solid-state materials. Fundamental magnetic properties of the material can be determined by studying charge transport in the presence of the external magnetic field and thermal gradient.

The relationship between the symmetries of the physical system plays a crucial role in explaining modern transport phenomena. Onsager (14) formulated an important relation between the response of a physical quantity α to a stimulus connected with the quantity β.

$$K_{\alpha\beta}(B) = \varepsilon_\alpha \varepsilon_\beta(-B), \tag{2.26}$$

where $\varepsilon_{\alpha,\beta} = \pm 1$specifies the symmetry property of α and $\beta$ concerning the operation of time-reversal. $B$ is any time-reversal ($T$) breaking field, so in the case of a ferromagnet, $B$ can be associated with magnetization. After applying this theorem to a conductivity tensor $\sigma_{ij}$ and the current response function, i.e. $\alpha \to J_i$ and $\beta \to J_i$, where $J_{i,j}$ are components of current density vector. Under the $T$ symmetry, the charge current is odd, thus $\varepsilon_{\alpha,\beta} = -1$. According to eq. (2.25) it holds that:

$$\sigma_{ij}(B) = \sigma_{ji}(-B) \tag{2.27}$$

The conductivity tensor is symmetric when no $T$ symmetry breaking field is present, i.e. $\sigma_{ij}(B = 0) - \sigma_{ji}(-B = 0) = 0$. The antisymmetric part $\sigma_{ij}(B) - \sigma_{ji}(B)$ can be finite only if the $T$ symmetry is broken (5). The $T$ symmetry of solids can be confirmed that way since the measurement of $\sigma_{ij}$ is straightforward.

A good example of a $T$ symmetry breaking field can be an external magnetic field in a conductive solid material. According to the drift-diffusion model $\sigma_{xy}(B) - \sigma_{yx}(B) = 2 \cdot \sigma_{xy}(B) \neq 0$ when the magnetic field is applied along the z-axis. This can be observed as an ordinary Hall effect. (69)

Ordinary Hall effect is a magnetotransport effect that can be described the following way: a magnetic field applied normally to the current direction in a conducting material produces a transverse force on the conduction electrons, and this force gives rise to a transverse-oriented Hall voltage. Ordinary Hall voltage is proportional to the applied magnetic field B because the Lorentz force acting on the conduction electrons is $F = e(E + v \times B)$. Electron accumulation will continue in the transverse direction until the field it generates is sufficient to stop the further flow of charge.

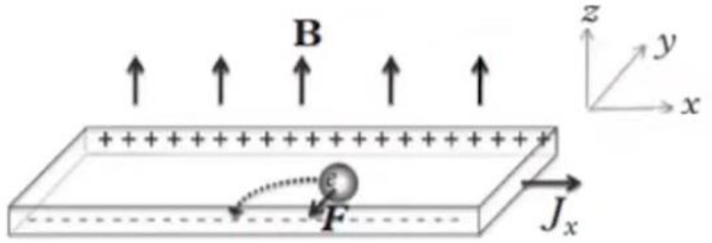


*Figure 7: Hall effect, $E_e$is Hall voltage, $F_y$ is Lorentz force, $B_z$ is applied magnetic field, $J_x$ is charge current. (15)*

Ordinary Hall voltage is proportional to the applied magnetic field $B$. Hall effect in the material, when assuming the single band approximation, can be described by the Hall coefficient (taking into account $j_x = ne^2\tau E_x$):

$$R_H = \frac{E_y}{j_x B} = \frac{-1}{ne}; \left[\frac{m^3}{C}\right] \qquad (2.28)$$

Where $j_x$ is the current density of the charge carriers, $B$ is the magnetic field and $E_y$ is the induced electric field. Since the Hall coefficient is inversely proportional to the carrier concentration $n$, its value for metals is much less than for semiconductors.

Expression for a specific transverse Hall resistivity can be written as:

$$\rho_{xy} = \frac{E_y}{j_x} = R_H B \qquad (2.29)$$

The effect of the Lorentz force acting on charge carriers also leads to a decrease of longitudinal resistivity $\rho_{xy}$, due to a deflection of the charge carriers. This effect is called ordinary magnetoresistance (OMR) and can be described by the ratio:

$$MR = \frac{\rho_{xx}(B) - \rho_{xx}(B=0)}{\rho_{xx}(B=0)} \qquad (2.30)$$

OMR follows a quadratic dependence on $B$ (16).

The Nernst effect is a thermoelectric analog to the Hall effect. The phenomenon can be observed when an electrical conductor is subjected to an external magnetic field and a thermal gradient normal to it. An electric field is induced normally to both.

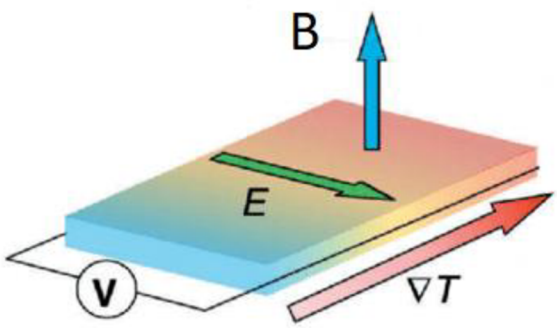


*Figure 8: Illustration of the ordinary Nernst effect, E is Nernst voltage, ∇T is temperature gradient, B is external magnetic field (17).*

The temperature gradient induces a charge carriers flux opposite to the thermal gradient. This is called the Seebeck effect and can be described as diffusion of high-energy carriers from the hot side producing entropy by drifting towards the cold end of the conductor. Drifting charge carriers are deflected by the Lorentz force induced by the external magnetic field.

The ordinary Nernst effect is characterized by the Nernst coefficient N:

$$E_y = NB_z \partial T / \partial x, \tag{2.31}$$

where $E_y$ is the transverse electric field, $\partial T / \partial x$ is a longitudinal temperature gradient, and $B_z$ is the out-of-plane magnetic field (see Figure 8). Nernst effect is not the only thermoelectrical effect in solid materials, for example, Ettingshausen effect manifests a conversion of the longitudinal electric current to the transverse temperature gradient or the Righi-Leduc effect that describes conversion of the longitudinal heat flow to the transverse temperature gradient.

Even though the electric and thermoelectric transport phenomena are driven by fundamentally different forces, there is a connection between the electric conductivity tensor $\overline{\sigma}$ and the thermoelectric tensor $\overline{\alpha}$.

Electric field and thermal gradient in equations (2.23) and (2.24) can be considered as perturbations to a Fermi-Dirac distribution of charge carriers, so the relations between $\overline{\sigma}$, $\overline{\alpha}$ and $\overline{\kappa}$ tensors can be found. An important relation is the Mott relation, which links the electric conductivity tensor $\overline{\sigma}$ and thermoelectric tensor $\overline{\alpha}$.

$$\overline{\alpha} = \frac{\pi^2}{3}\frac{k_B}{e} k_B T \frac{\partial \overline{\sigma}}{\partial \epsilon}\Big|_{\epsilon=\epsilon_F} \tag{2.32}$$

where $\epsilon$ is the energy of the carriers ($\epsilon_F$ is the Fermi energy) and T is temperature.

Nernst coefficient *N*, mentioned in the equation (2.30) relates to $\alpha_{xy}$ as (18):

$$N = B_z \frac{\alpha_{xy}}{\sigma_{xx}} \tag{2.33}$$

The Mott relation then connects the off-diagonal elements of the $\overline{\alpha}$ and $\overline{\sigma}$ tensors, which in the presence of the magnetic field connects ordinary Nernst and Hall effects.

### 2.2.4 Anomalous Hall and anomalous Nernst effect

In magnetic materials the Hall resistivity $R_H$ (transverse electric field per unit longitudinal current density) is different: after initially increasing with the field the Hall resistivity saturates at large fields to some value, which is nearly independent of the field:

$$\rho_{AH} = R_0 B + \mu_0 R_e M, \qquad (2.34)$$

where $R_0$ is the ordinary Hall coefficient, $R_e$ is referred to as an anomalous Hall coefficient, which is also dependent on temperature, as well as a variety of materials-specific parameters. This additional contribution to the magnetization $M$ is called the anomalous Hall effect (AHE) and is observed in magnetically ordered materials with broken time reversal symmetry.

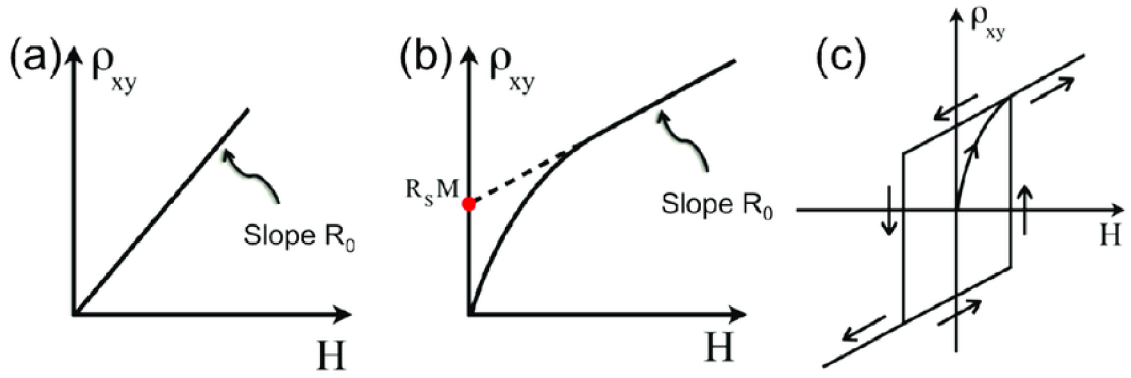


*Figure 9: Typical behaviors of the Hall and anomalous Hall effects. The Hall resistivity ρ xy is plotted versus external magnetic field H. (a) The ordinary Hall effect; (b) The anomalous Hall effect; and (c) The hysteresis loop measured from the anomalous Hall effect (19).*

Despite this phenomenological relationship, a microscopic theory of AHE turned out to be particularly difficult to formulate. Conventionally, the AHE has been ascribed to spin-orbit interaction and the spin polarization of conduction electrons, which result in asymmetry in terms of orbital angular momentum (20), or to the asymmetric skew scattering of conduction electrons by the fluctuation of localized moments (21).

The AHE theory of Karplus and Luttinger (20) has been recently reformulated (5) using the concept of Berry's phase and Berry's curvature (22). Berry's phase is an additional phase of the electron's wave function arising in the system with multiple time-dependent parameters in the Hamiltonian. Berry curvature is then a vector field in the space of the time-dependent parameters, with Berry's phase being its integral over a closed trajectory (23). A usual example of the topological Berry's phase is the rotation of a spinor.

Consider the $s = 1/2$ angular momentum aligned to a magnetic field, which rotates adiabatically so that the spinor remains aligned to it. At the end of the loop, the spinor acquires a complex phase factor $exp(i\phi)$. Likewise, ordinary vectors are basically $s = 1$ spinors, the parallel transport of ordinary vectors on a sphere should also give interesting geometric phases. Indeed the Berry phase for a transport along a sphere diameter yields a Berry phase of $2\pi$, i.e. a full rotation, equivalent to no rotation at all $[exp(i4\pi/2) = exp(i2\pi) = 1]$. Instead, a smaller path enclosing one eight of the sphere yields the geometric phase of $4\pi/8 = \pi/2 = 90°$ illustrated below.

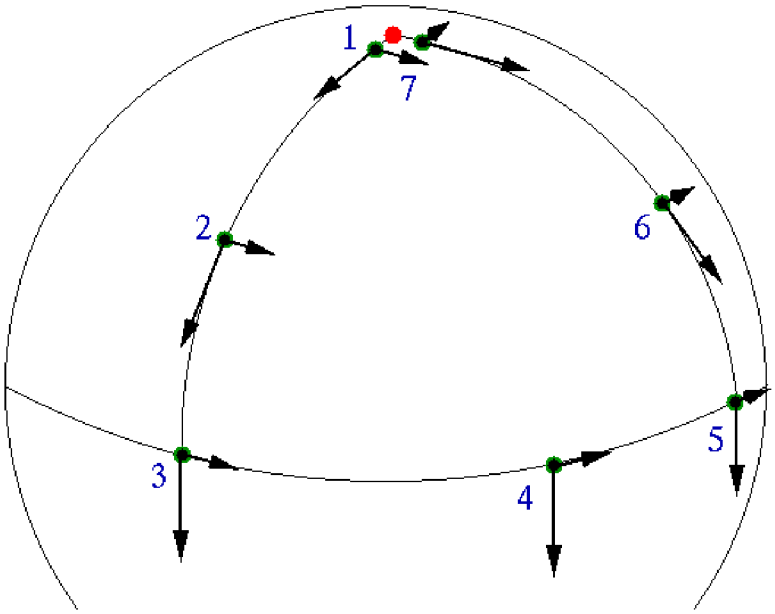


*Figure 10: Illustration of a topological Berry's phase (24)*

Berry's curvature in the momentum space has two properties important for this work: firstly, it is directly proportional to the anomalous Hall conductivity, and secondly, Berry's curvature can only have a non-zero value when the combined time-reversal and mirror reflection symmetry is broken (7).

In the case of Bloch waves in crystals, the Berry curvature modifies the group velocity by introducing an anomalous term (25).

$$\dot{r} = \frac{1}{\hbar}\frac{\partial \epsilon_n(k)}{\partial k} + \frac{e}{\hbar}E \times \Omega_n(k) \qquad (2.35)$$

In the absence of the second term on the right side of this equation, the group velocity $\dot{r}$ is defined by the energy dispersion $\epsilon_n(k)$ of a band indexed $n$. The presence of a finite $\Omega_n(k)$ affects various transport properties of electrons in the crystal.

It was pointed out (7) that AHE can appear in noncollinear antiferromagnets with zero net magnetization when certain common symmetries are absent. The magnitude of the resulting AHE is comparable to AHE in elemental transition metal ferromagnets (Fe, Co, Ni). The AHE has been experimentally identified in several noncollinear antiferromagnets $Mn_3X$ (X being Ir (7), Sn (26), Ge (27), Ga (28) with a kagome lattice of magnetic Mn atoms, and in antiperovskite materials such as $Mn_3NiN$ (29).

A recent work by Smejkal et al. (30) suggested a mechanism of time-reversal symmetry breaking even in antiferromagnets with collinear spin structure, so-called altermagnets (see chapter 2.3). The resulting anomalous Hall effect (called crystal Hall effect is some publications (31)) can be as large as in ferromagnets and spontaneous (i.e. present in zero magnetic field).

Another mechanism of the $T$ symmetry breaking is proposed for ferromagnets and antiferromagnets with nontrivial spin structures (32). In the materials with non-parallel spin in the individual sublattices, it is convenient to introduce the spin chirality $\kappa = \sum S_i \cdot (S_k \times S_i)$, with $S_{i,k,l}$ being three magnetic moments in the magnetic lattice. $\kappa$ is zero for collinear ordering. Finite spin chirality can induce Berry's curvature in real space, resulting in the so-called *topological Hall effect (THE)*. THE can be observed even in materials without strong spin-orbit interactions (33). THE has been observed in noncollinear antiferromagnet $Mn_3Sn$ (19), the noncollinear phase of antiferromagnetic $Mn_5Si_3$ (33), and various double-exchange ferromagnets (34).

Nernst effect also has its anomalous counterpart. Applying a thermal gradient to a ferromagnet generates a voltage that is perpendicular to both the heat flow and the magnetization. That phenomenological description of ANE holds for ferromagnets with a finite net magnetization. In a theoretical study of ANE, Xiao and colleagues (25) argued that even though the force produced by a thermal gradient is statistical and therefore intrinsically macroscopic (in contrast to the one induced by an electric field), a finite Berry's curvature generates an anomalous transverse thermoelectric response $\alpha_{xy}^A$, which magnitude is linked to the anomalous Hall conductivity $\sigma_{xy}^A$:

$$\alpha_{xy}^A = \frac{\pi^2}{3}\frac{k_B}{e} k_B T \left.\frac{\partial \sigma_{xy}^A}{\partial \epsilon}\right|_{\epsilon=\epsilon_F} \qquad (2.36)$$

This is the same relation as (2.31), which links the ordinary version of the two effects in case with no spin-orbital interaction. In ferromagnetic solids, the measured values of ANE and AHE were reported to agree with the Mott formula (35) (36) (37).

However, there is an ongoing discussion about the general validity of the Mott relations in the material with a nontrivial topology of the electronic bands. It was proposed that the ANE could be sensitive to the electronic states which do not affect AHE, that assumption is not yet confirmed experimentally. ANE is considered to be determined by Berry's curvature at $E_F$, in contrast to AHE, which is obtained by the integration of Berry's curvature for all of the occupied bands. Thus, the observation of a large AHE does not guarantee the observation of a large ANE.

## 2.3 Anomalous Nernst effect in magnetic materials

The anomalous Nernst effect was observed and measured in a huge variety of magnetic materials. This chapter will introduce some of the existing measurements of ANE in ferromagnetic and antiferromagnetic and compare them.

Mizuguchi's group published several papers on ANE measurements in ferromagnetic alloys including FePt (38), FePd, MnGa, $Mn_2Ga$ and Co/Ni multilayer films (39). High values of ANE were also reported for $Fe_3Ga$ (40), $Fe_3Pt$ (41), $Fe_3GeTe_2$ (42), MnAl (43) and MnBi (44). Some Kagome ferromagnets incl. $Co_3Sn_2S_2$ (45) and $UCo_{0.8}Ru_{0.2}Al$ (46) also demonstrate huge coefficients of ANE.

Conventionally, the ANE was considered proportional to magnetization and, thus, observed only in ferromagnets. Recent studies show that ANE can also be realized in noncollinear antiferromagnets. With zero or vanishingly small magnetization due to the topologically nontrivial Berry curvature near the Fermi energy (47) (48) (49) (50) (51). ANE was observed in chiral antiferromagnets $Mn_3Sn$ (48) and $Mn_3Ge$ (49), antiperovskite structure antiferromagnet $Mn_3SnN$, canted antiferromagnet $YbMnBi_2$ (52) and other antiferromagnets, including $NdMn_2Ge_2$ (53), $Mn_3NiN$ (29).

Comparison of the ANE coefficients of some of the described ferromagnetic and antiferromagnetic materials is shown in Figure 11.

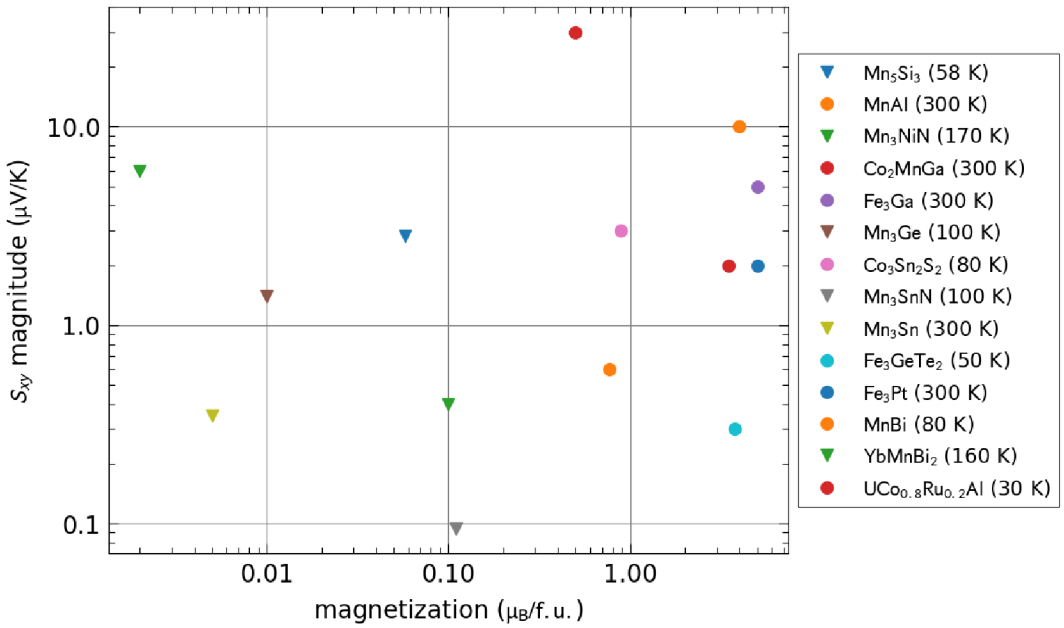


*Figure 11: Comparison of ANE coefficients vs. magnetization for some ferromagnetic and antiferromagnetic materials. Ferromagnetic materials are marked by circles, antiferromagnets are marked by triangles.*

## 2.4 Methods of Nernst effect measurements

In that part, we will describe some of the methods used to measure ANE coefficient in different materials. A necessary part of the measurement is creating a temperature gradient in the sample, which can be achieved by various methods.

### 2.4.1 In-plane methods

The main method of creating of thermal gradient in the in-plane direction is Joule heating of the sample. The external resistor connected to the sample using thermal conductive

compound can be used for that as described in paper (54), configuration is shown in Figure 12.

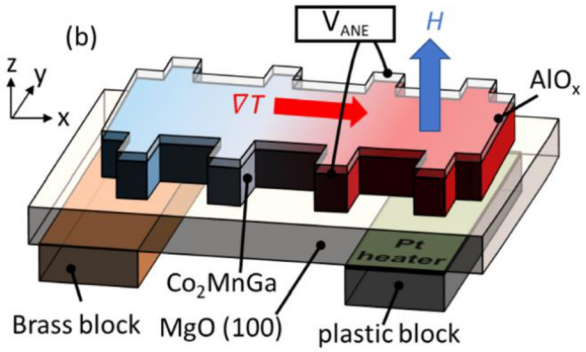


*Figure 12: Configuration for ANE measurement involving separate macroscopic heater (54)*

Another option is defining a microscopic heater right on the sample using the lithography technique as described in (29).

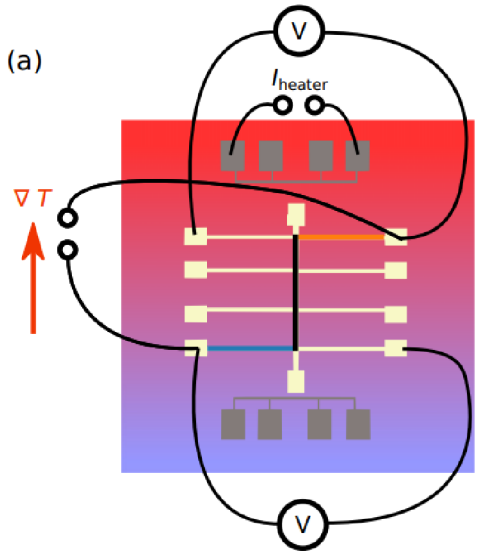


*Figure 13: Configuration for ANE measurement involving patterned on-chip heater (29)*

That configuration lets us reduce the mistake induced by different geometry factors that are hard to define precisely (for example: glue layer thickness, positioning of the heater under the sample, etc.). However, the magnitude of the temperature gradient here is limited, on-chip thermometers are less powerful than the macroscopic ones.

### 2.4.2 Out-of-plane methods

Measuring the ANE in the out-of-plane direction is more complicated than in the in-plane direction. The value of the temperature gradient is difficult to measure using traditional on-chip Pt thermometers, out-of-plane measurements would require multiple thermometers in different layers isolated from each other. Paper (55) describes the multilayer structure used to measure ANE in the sample, the spin detection layer was used as a thermometer.

Another option for out-of-plane measurements is using localized heating to create a temperature gradient. Paper (56) describes the method of inducing a local temperature gradient by a heated AFM tip. That method also enables us to map the thermoelectric effect and provide information about the domain structure of the sample. Using laser pulses to induce the temperature gradient also gives consistent results (57).

# 3 Experimental part

To determine how the substrate and geometry affect the anomalous Nernst effect measurements, we have fabricated 7 different devices on 4 different single-crystal substrates: $Al_2O_3$ (0001), Si (100), $SrTiO_3$ (100), MgO(100). Those substrates were chosen due to differences in their thermal conductivity, which lets us observe its effect on the anomalous Nernst signal. Devices were fabricated by a two-step lithography process.

## 3.1 Device fabrication

In this part, we will describe the methods used to fabricate devices for anomalous Nernst effect measurement.

Photolithographic process consisted of three phases: coating the substrate by a suitable photoresist, patterning the resist using the photolithography equipment and developing the resist by a suitable developer.

We have used the ma-P 1210 series positive photoresist by Micro Resist Technology GmbH company, which was coated onto the substrate by spincoating technique using the parameters recommended by the manufacturer, i.e. with the velocity of 4000 rot/s and the acceleration 1500 rot/s$^2$. After the spincoating, the resist was tempered on the 100 °C hot plate for 100 s.

The photoresist was then patterned using the Durham Magnetooptics ML-3 Microwriter using the 365 nm wavelength and 80 mJ/cm$^3$ irradiation dose. After that, the resist was developed using the recommended developer (ma-D 331) for 40 seconds, then rinsed in distilled water to stop the developing. Obtained structures were then cleaned in oxygen plasma using the Diener Femto low-pressure plasma chamber to descum the substrate of the remaining developed photoresist and organic contaminations.

After that, the $Ni_{77}Fe_{14}Cu_5Mo_4$ ferromagnetic alloy was sputtered onto the substrates by magnetron sputtering. Permalloy was sputtered onto every sample in argon atmosphere of 2,5 mtorr with 15 W source power for 7 minutes. The resulting layer of alloy was 55-65 nm thick, which was measured by the Dektak profilometer.

During the second step, the on-chip platinum thermometers were also fabricated by a lift-off technique using the same process parameters. Platinum was sputtered onto the samples from a platinum sputtering target with the argon pressure of 2.5 mtorr and the sputtering source power of 15 W. The resulting platinum layer was 60-65 nm thick.

## 3.2 Experimental configurations for the anomalous Nernst effect measurements.

### 3.2.1 Macroscopic heater configuration

We used the following configuration to investigate the influence of the sample substrate on the anomalous Nernst signal. We therefore fabricated four samples in this configuration, each with one of the above listed substrates. The schematic illustration of

the device configuration is shown at Figure 14, chip layout is shown in Figure 15, real photo of the device is shown in Figure 16.

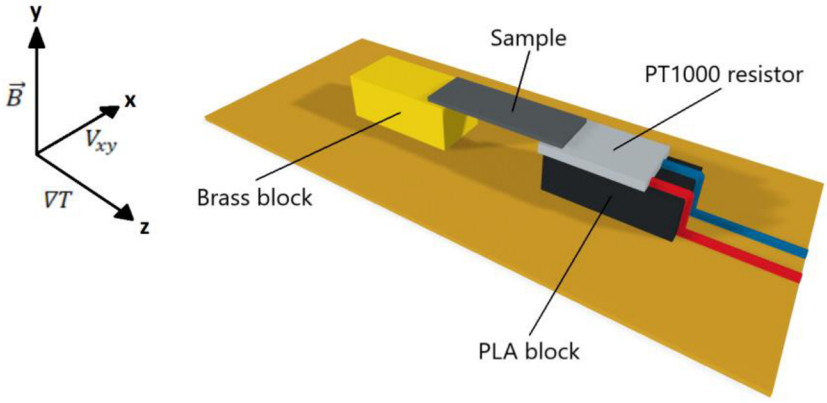


*Figure 14: Schematic image of the macroscopic heater device configuration*

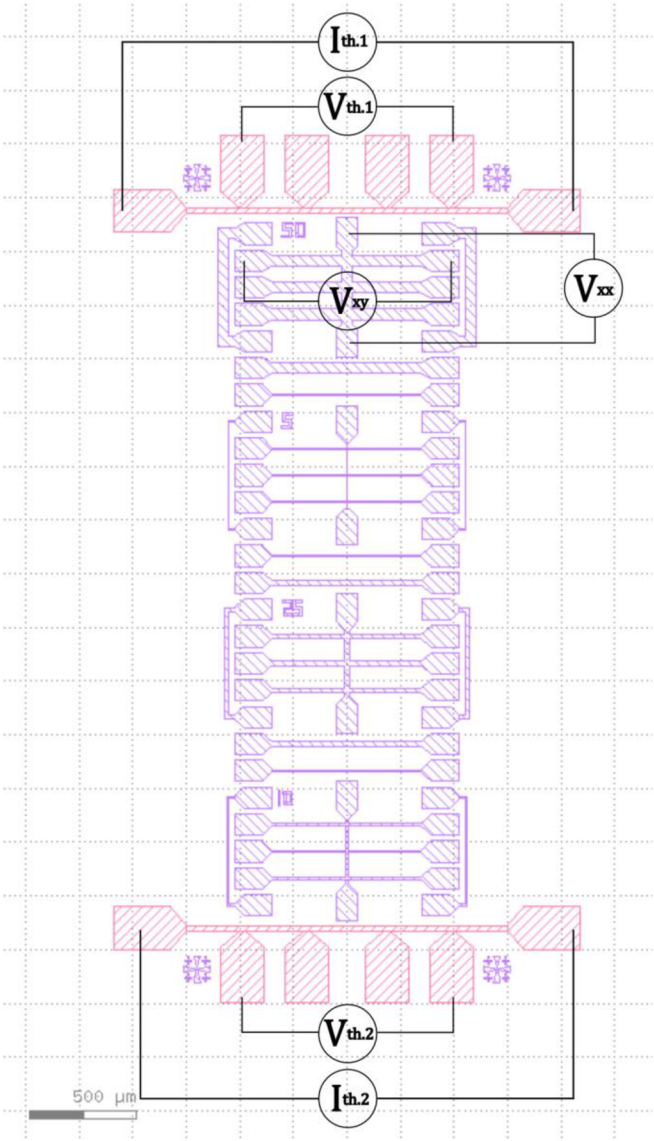


*Figure 15: Layout of the macroscopic heater configuration chip (Red colour – Pt, magenta – permalloy)*

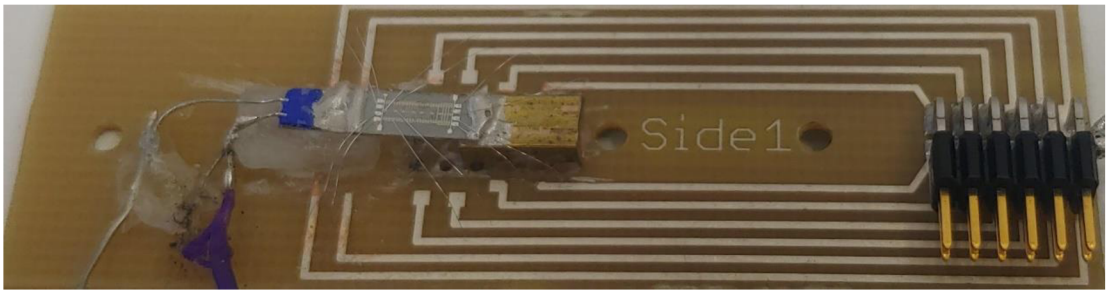


*Figure 16: Photo of the macroscopic heater configuration sample*

The sample is heated from the bottom side by a calibrated 1000Ω platinum resistor. The resistor is mounted onto the 3D-printed PLA block using the cyanoacrylate glue, so the heater is thermally insulated from the chip carrier. The other side of the sample is connected to a brass block by a thermoconductive epoxy glue, therefore creating a heat sink.

This configuration allowed us to generate an in-plane temperature gradient. We determined the magnitude of the gradient by measuring the resistance of the platinum stripes located on the heater and heatsink sides of the sample. The resistance temperature dependence of the platinum stripes was calibrated by slow temperature sweeps. Simultaneously, the sample temperature was precisely determined by a temperature sensor PT100 (type PT-385). The temperature gradient magnitude was then calculated as:

$$|\nabla T| = \frac{T_{heater} - T_{heatsink}}{d}$$

During the measurement, we detected thermovoltage in the permalloy layer transverse and longitudinal to the applied temperature gradient. The voltages were measured on the marked ($V_{xx}$ and $V_{xy}$) device in Figure 15. The bars were electrically connected to the chip carrier by aluminum bonds.

### 3.2.2 On-chip heater

Another configuration for the measurement of the ANE we evaluated is the on-chip-heater configuration. This configuration consists only of a chip (layout is shown at Figure 17, real photo at Figure 18) glued to the PCB plate by non-conductive epoxy glue at the heater side and conductive one at the other side, which also helps to achieve a higher thermal gradient. The sample is heated on one side by a deposited platinum heater. The temperature on both ends of the sample was measured the same way as in the macroscopic heater configuration. Even though the resistance of the on-chip heater is significantly lower than the resistance of the macroscopic heater, we achieve a temperature gradient of 0.6 K in this configuration. The Nernst and Seebeck voltage is measured on the transverse and longitudinal strips. That configuration is more stable during the measurement because the overall thermal capacity is lower, so it takes less time to stabilize the heater power and the temperature gradient.

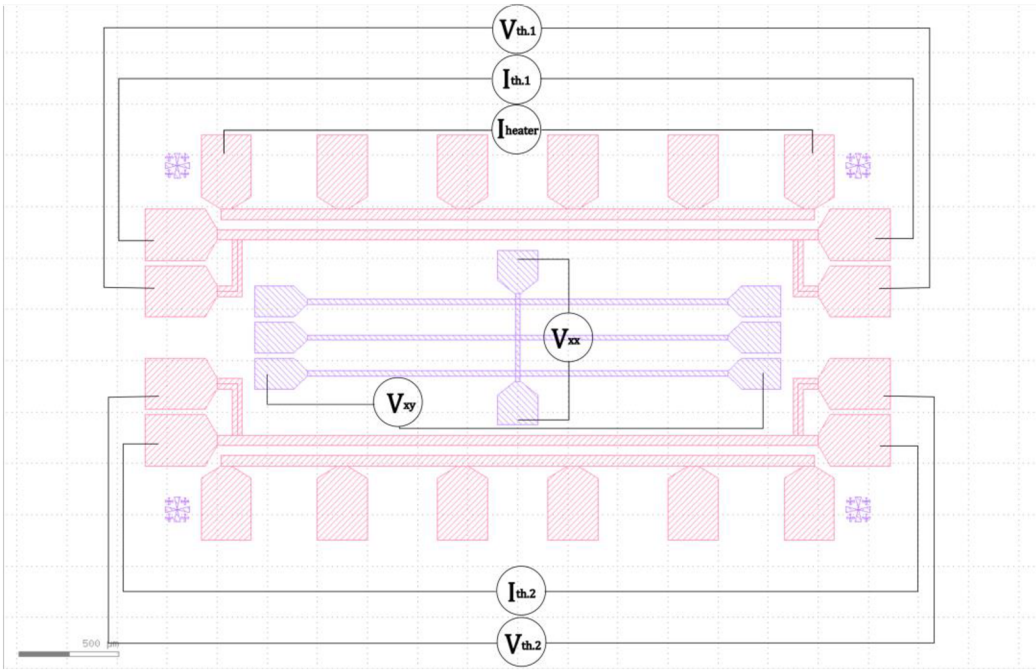


*Figure 17: Layout of the on-chip heater configuration (Red colour – Pt, magenta – permalloy)*

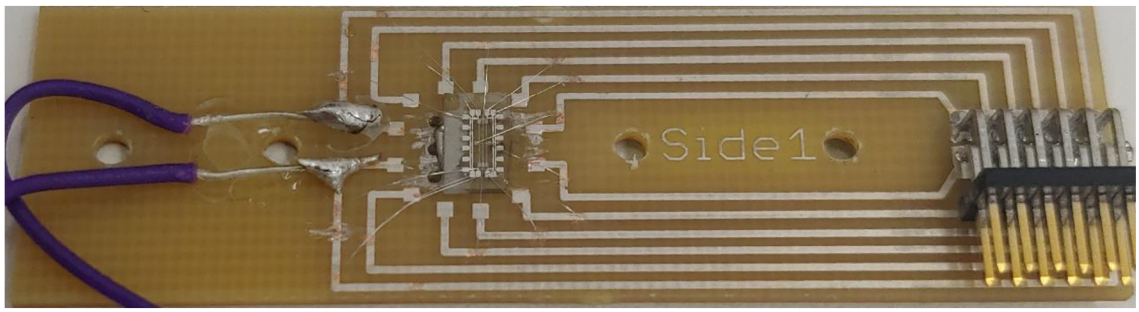


*Figure 18: Photo of the on-chip heater configuration sample*

### 3.2.3 Out-of-plane measurements

To measure out-of-plane thermal gradient we used a chip layout shown in Figure 19 (real photo at Figure 20), with the PT1000 platinum resistor glued on top of it. Applying current to the resistor therefore creates an out-of-plane temperature gradient, and the Nernst effect is measured on the ends of the alloy stripes. That configuration does not allow us to measure the temperature gradient directly, but it can be calculated using the data we obtained by measuring the samples of the different configuration (see the details in the results section).

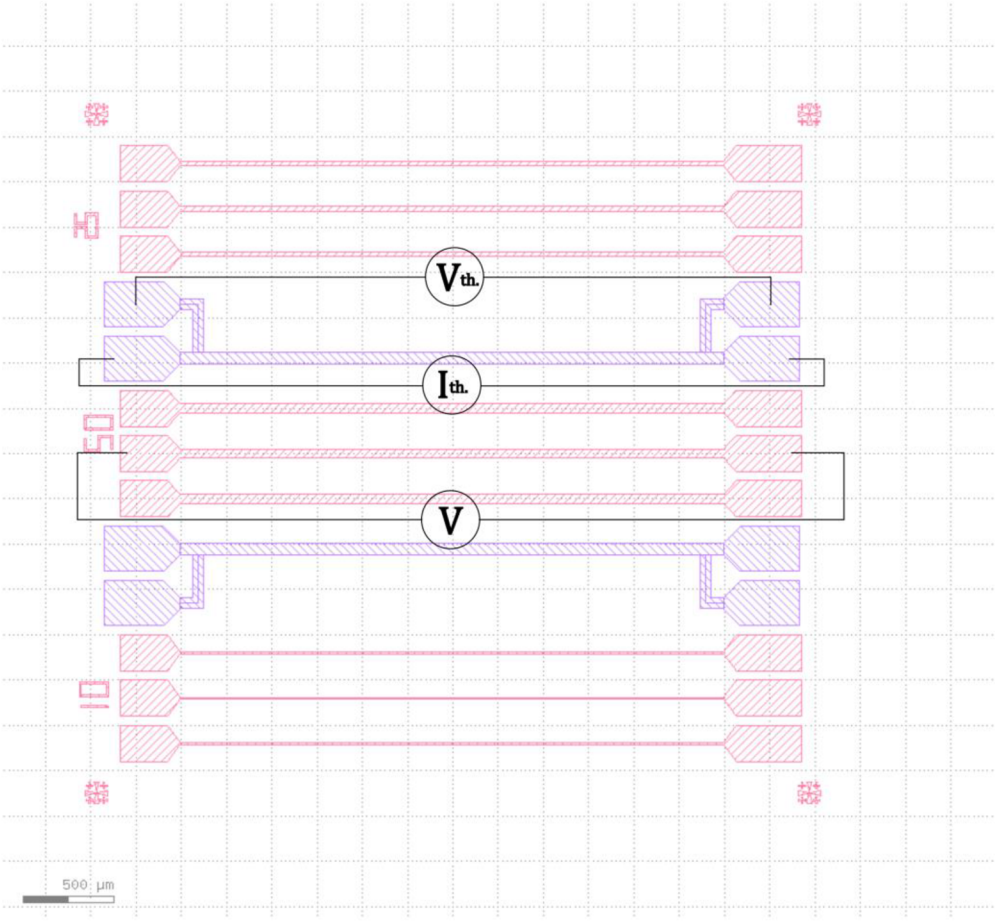


*Figure 19: Layout of the out-of-plane measurement configuration (Red colour – Pt, magenta – permalloy)*

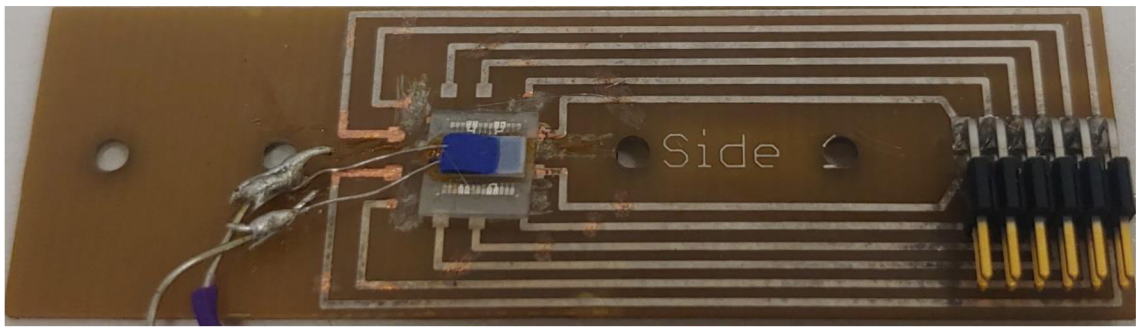


*Figure 20: Photo of the out-of-plane measurement configuration sample*

### 3.2.4 Alternating thermal gradient configuration

Alternating thermal gradient configuration, in contrast to other configurations, uses two on-chip platinum heaters which are switched on and off alternately, therefore reducing the error created by geometry factor. The chip layout is shown in Figure 21 and the real photo of the sample is in Figure 22 The configuration consist of a chip glued to the PCB plate by non-conductive epoxy glue at the heater side and conductive one at the other

side. For each measurement point, current is applied to heater for 5 seconds to ensure the stabilization of the temperature gradient. When the gradient is stable, we measure transverse voltage on our permalloy device and then reverse the direction of the temperature gradient by switching off the heater H1 and turning on the heater H2. The platinum thermometers are calibrated in the same way as in the macroscopic and on-chip heater configuration.

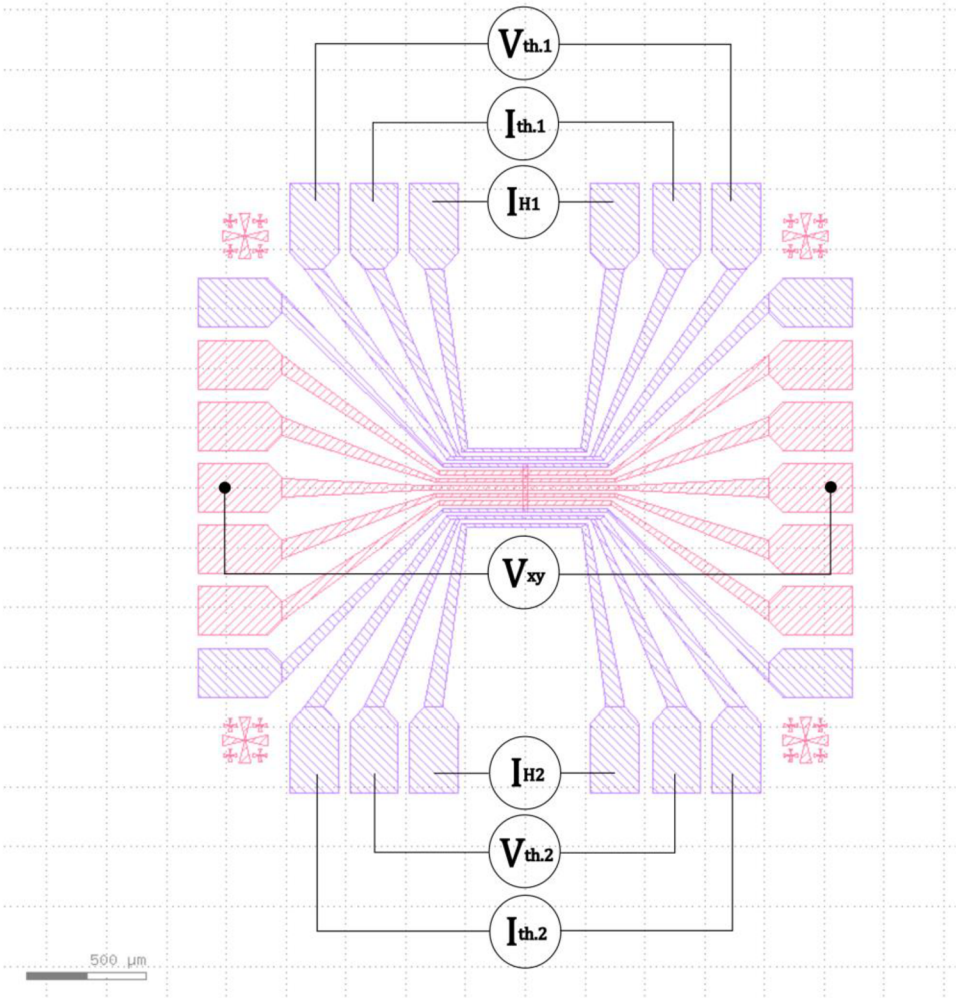


*Figure 21*: *Layout of the alternating thermal gradient configuration chip (Red colour – Pt, magenta – permalloy)*

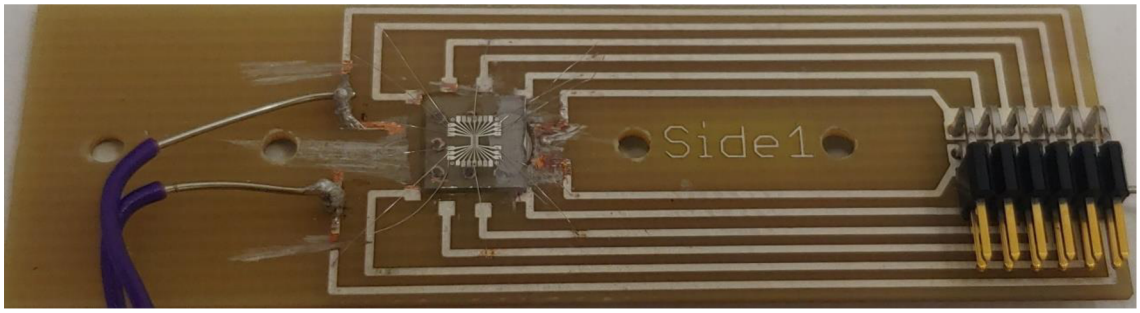


*Figure 22 Photo of the alternating gradient configuration sample*

## 3.3 Nernst effect measurements.

The anomalous Nernst effect was measured in our samples in an Oxford Instruments INTEGRA cryostat with the integrated superconductive electromagnet and variable temperature insert (VTI) (Figure 23). The VTI can reach temperatures between 1.2 and 310 K. We measured the Nernst, Hall, and Seebeck signals as a function of magnetic field applied along the y-axis. To do so, we were gradually changing the magnetic field between 0.6 and -0.6 T with the step of 0.01 T. The maximum field value was chosen to reach the magnetic saturation of our permalloy samples (the corresponding magnetic field was determined by the SQUID magnetometry).

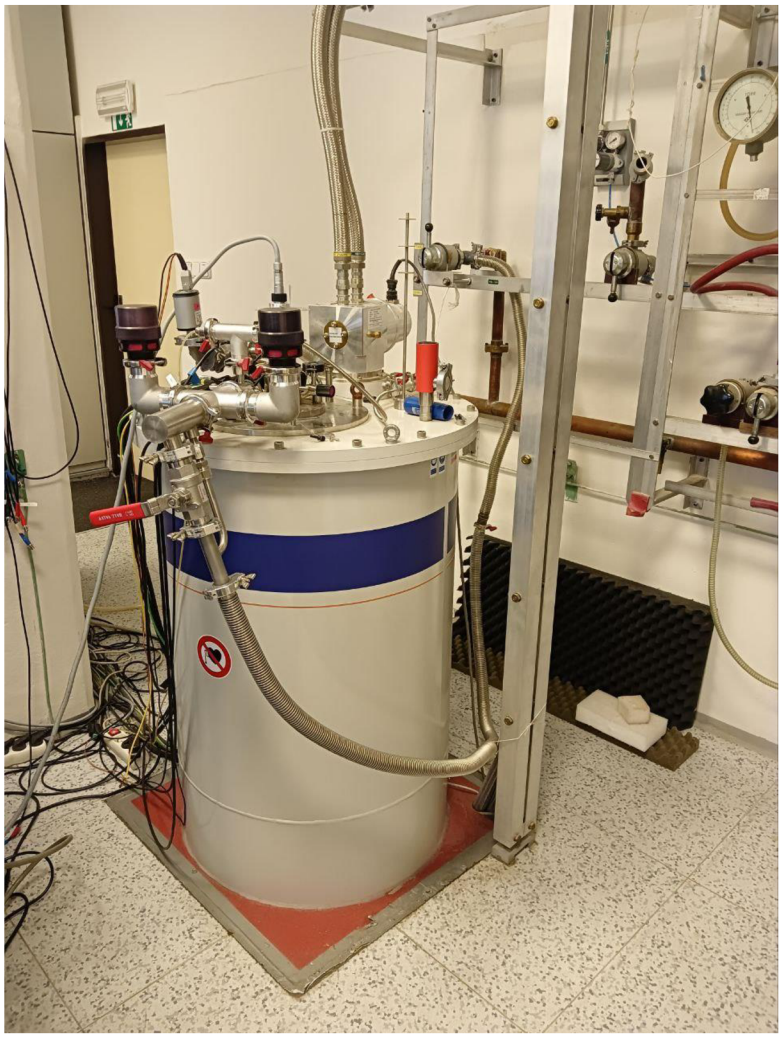

*Figure 23: Oxford Instruments INTEGRA cryostat with the integrated superconductive electromagnet and variable temperature insert*

The voltage at the ends of the permalloy strips was measured using two Keithley 2182A nanovoltmeters (one for the longitudinal and one for the transverse direction). The temperature dependence of the resistance of the PT100 and on-chip thermometers was measured using the Keithley DMM6500 multimeters in a 4-wire configuration.

We also measured the Hall effect on the same samples, by applying current in the longitudinal direction and collecting the Hall signal in the transverse direction.

### 3.3.1 Thermometer calibration

The measured temperature dependences of the platinum stripe resistances were plotted as functions of the sample temperature, which was measured by a PT100 thermometer. Temperature can be calculated from the PT100 resistance using the Callendar-Van Dusen equation:

$$T = \frac{-A+\sqrt{A^2-4B\left(1-\frac{R_t}{R_0}\right)}}{2B}, \tag{3.1}$$

where $A = 3.9827 \cdot 10^{-3}, B = -5{,}875 \cdot 10^{-7}, R_0 = 100$ for this particular type of the thermometer.

An example of the calibration curves for both on-chip thermometers is shown in Figure 24.

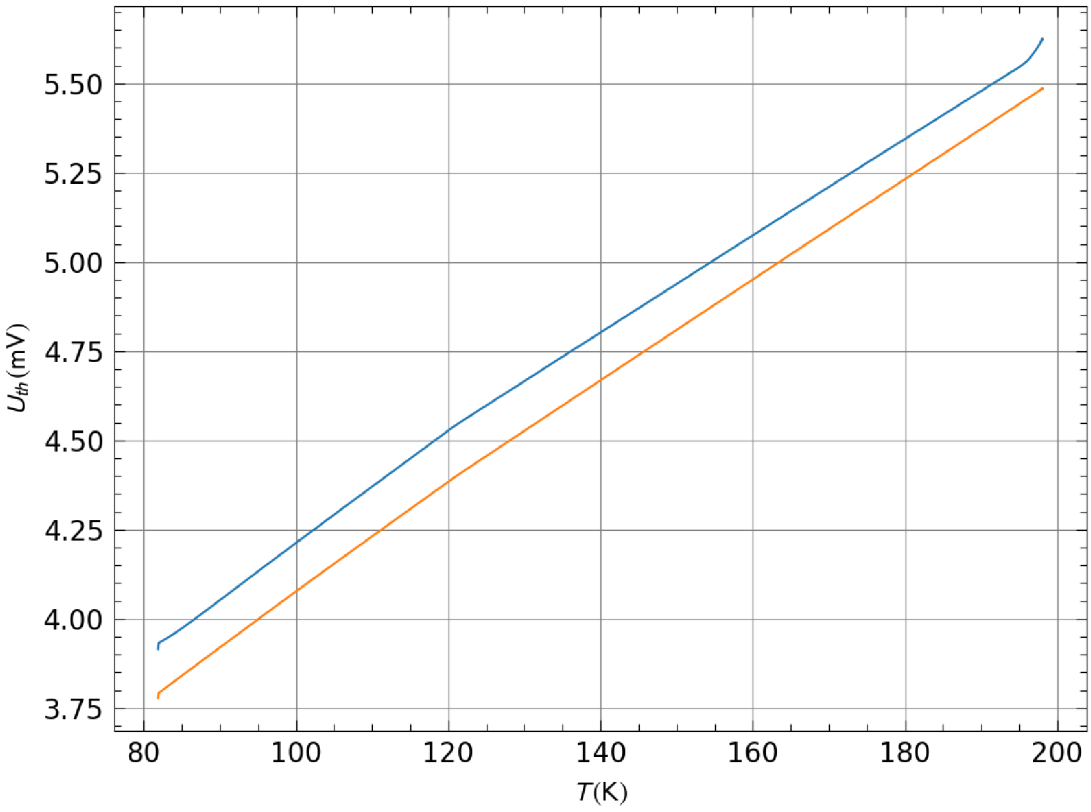


*Figure 24: Calibration curves of two on-chip thermometers (STO macroscopic heater sample)*

### 3.3.2 Signal symmetrization and calculation of the Nernst and Hall coefficients

To get rid of the unwanted factors that can affect the magnitude of the measured transverse signal, we have isolated the odd and even components of the measured data. Those factors include geometrical misalignment of the transverse contacts with respect to the current direction, or misalignment of the sample plane in the magnetic field, which yields an out-of-plane contribution. (58)

In a described field-sweep experiment, odd and even parts of data can be obtained as:

$$\rho_{\leftarrow}^{even}(H) = \frac{\rho_{\leftarrow}(H) + \rho_{\rightarrow}(-H)}{2}, \rho_{\leftarrow}^{odd}(H) = \frac{\rho_{\leftarrow}(H) - \rho_{\rightarrow}(-H)}{2}$$

$$\rho_{\rightarrow}^{even}(H) = \frac{\rho_{\rightarrow}(H) + \rho_{\leftarrow}(-H)}{2}, \rho_{\rightarrow}^{odd}(H) = \frac{\rho_{\rightarrow}(H) - \rho_{\leftarrow}(-H)}{2} \quad (3.2)$$

where $\rho_{\rightarrow}(H)$ and $\rho_{\leftarrow}(H)$ are the subsets of the data obtained for a decreasing or increasing magnetic field magnitude. (58)

After the antisymmetrization procedure, the odd part of the data can be considered the clear Nernst signal. Nernst coefficient can then be calculated as:

$$S_{xy} = \frac{V_{xy}^{odd}/l_{xy}}{|\nabla T|},$$

where $l_{xy}$ is the length of the transverse contact, $|\nabla T|$ is the magnitude of the temperature gradient, $V_{xy}^{odd}$ is the odd part of the data obtained from the nanovoltmeter (59).

Hall coefficient is calculated using the following equation:

$$\rho_{xy} = \frac{V_{xy}^{odd} * h}{I_{xx}},$$

where $V_{xy}^{odd}$ is the odd part of the data obtained from the nanovoltmeter, $h$ is permalloy layer thickness, $I_{xx}$ is the longitudinal current.

# 4 Results and discussion

## 4.1 Sample characterization

### 4.1.1 Structural characterization

To study the structural properties of our peramalloy samples, we employed the techniques of x-ray diffraction (XRD) and x-ray reflectometry (XRR). Data was obtained using the Malvern Panalytical X-ray diffractometer (Figure 25).


*Figure 25 Malvern Panalytical Empyrean X-ray diffractometer*

Figure 26 shows the angular distribution of the x-ray diffracted intensity as obtained via XRD.

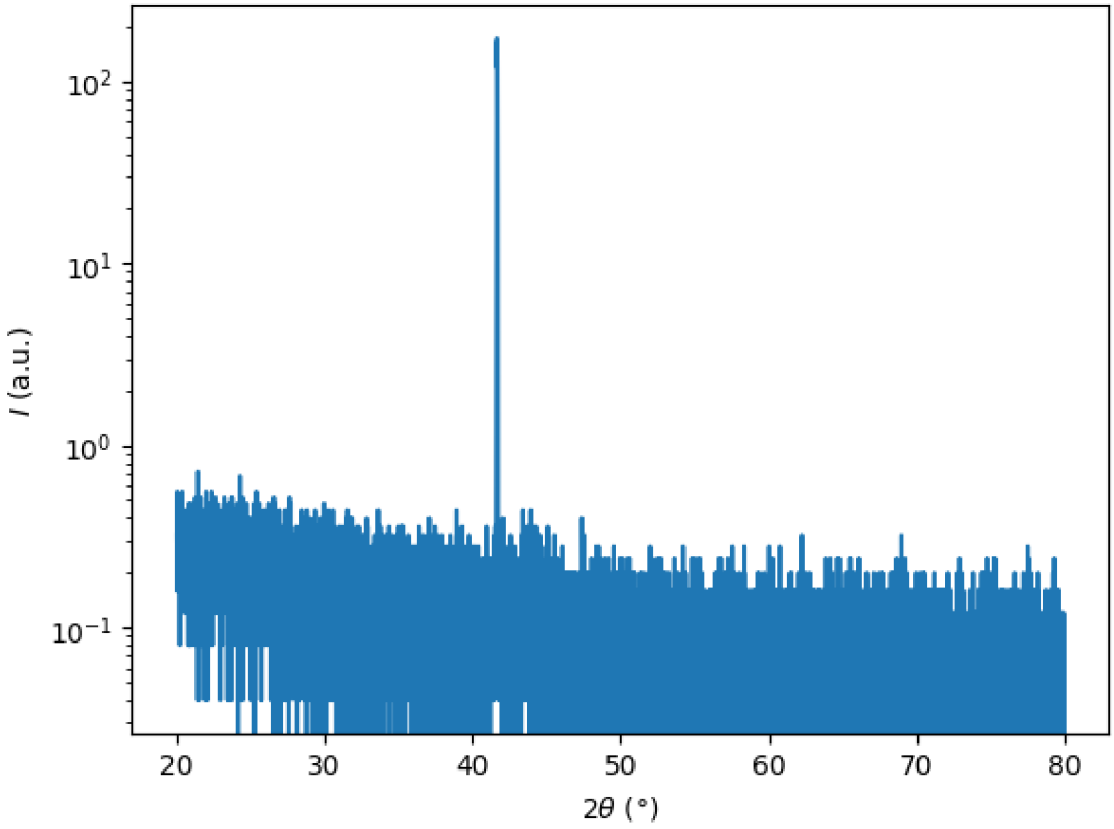


*Figure 26 XRD pattern of permalloy sample on $Al_2O_3$ substrate*

Single peak at 2θ = 42° responds to the $Al_2O_3$ substrate in the (0006) direction. As any other peaks are absent, we can state that permalloy film is highly polycrystalline or amorphous.

The thickness of our deposited layers can be precisely determined by XRR. To do so, we measured the XRR dependence of reflected intensity on the incidence angle as shown in

Figure 27. By fitting the dependence via the xrayutilities Python package, we obtain the permalloy film thickness of 68.4 nm with a 3 nm oxide surface layer.

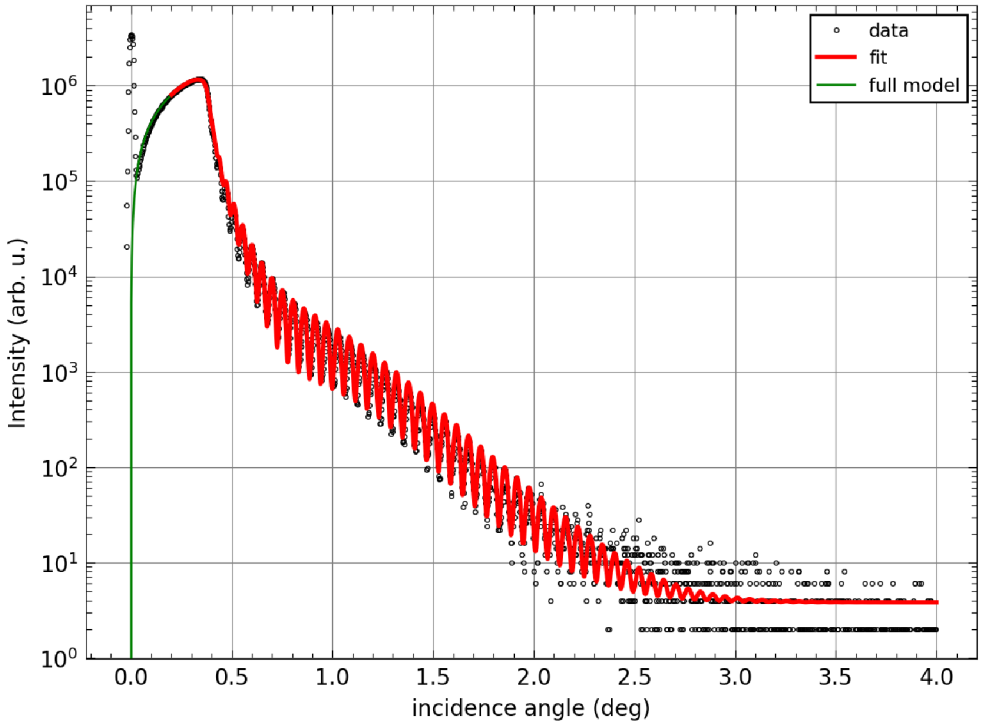


*Figure 27 XRR dependence of permalloy sample on $Al_2O_3$ substrate*

### 4.1.2 Magnetic characterization

Characterization of the samples' magnetic properties was made using the SQUID magnetometry technique in the MPMS7 XL SQUID magnetometer (Figure 28). Magnetometer is designed for sensitive magnetization and AC susceptibility measurements, and custom extensions allow the application of AC or DC fields for investigation of the magnetoelectric response. (60)

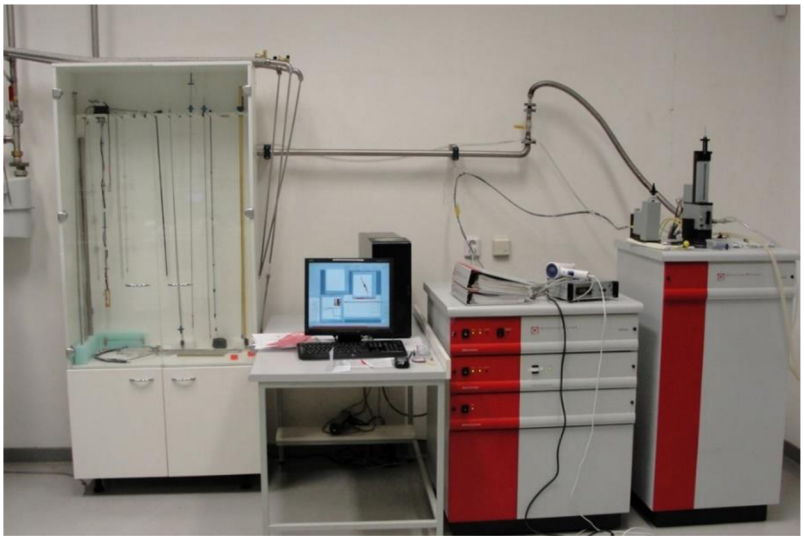

*Figure 28: MPMS7 XL SQUID magnetometer*

We measured the magnetic field dependence of the magnetic moment of a permalloy sample on $Al_2O_3$ substrate in two configurations: with the magnetic field applied in-plane and out-of-plane. The magnetization of our thin layers was calculated by dividing the measured magnetic moment by the layer volume and subtracting the linear-in-field diamagnetic contribution of the $Al_2O_3$ substrate. The resulting magnetization dependencies are shown in Figure 29.

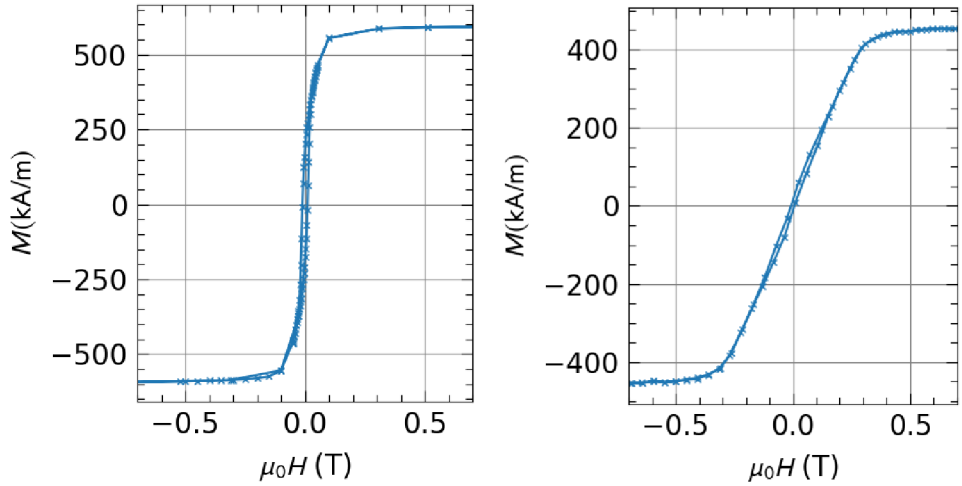


*Figure 29: Magnetization curve of permalloy sample on $Al_2O_3$ substrate. Left side: magnetic field applied in the sample plane, right side: magnetic field applied out of the sample plane.*

Out-of-plane direction is considered magnetically hard direction with a saturation field of 0.35 T. In-plane direction is magnetically soft with the saturation field of 0.1 T. Magnitude of the magnetic moment is 420 and 540 kA/m, which corresponds to the results obtained by other researchers for permalloy (61).

### 4.1.3 Hall measurements

As a part of the samples' characterization, we conducted an experiment to characterize the magnetic field dependence of transverse resistivity for permalloy grown on different substrates. We used the same macroscopic heater configuration samples which will be used for the ANE experiments, connecting the longitudinal contact of permalloy stripe to the current source and measuring the transverse voltage. Graphs of transverse resistivity in dependence on the applied magnetic field are shown in Figure 30.

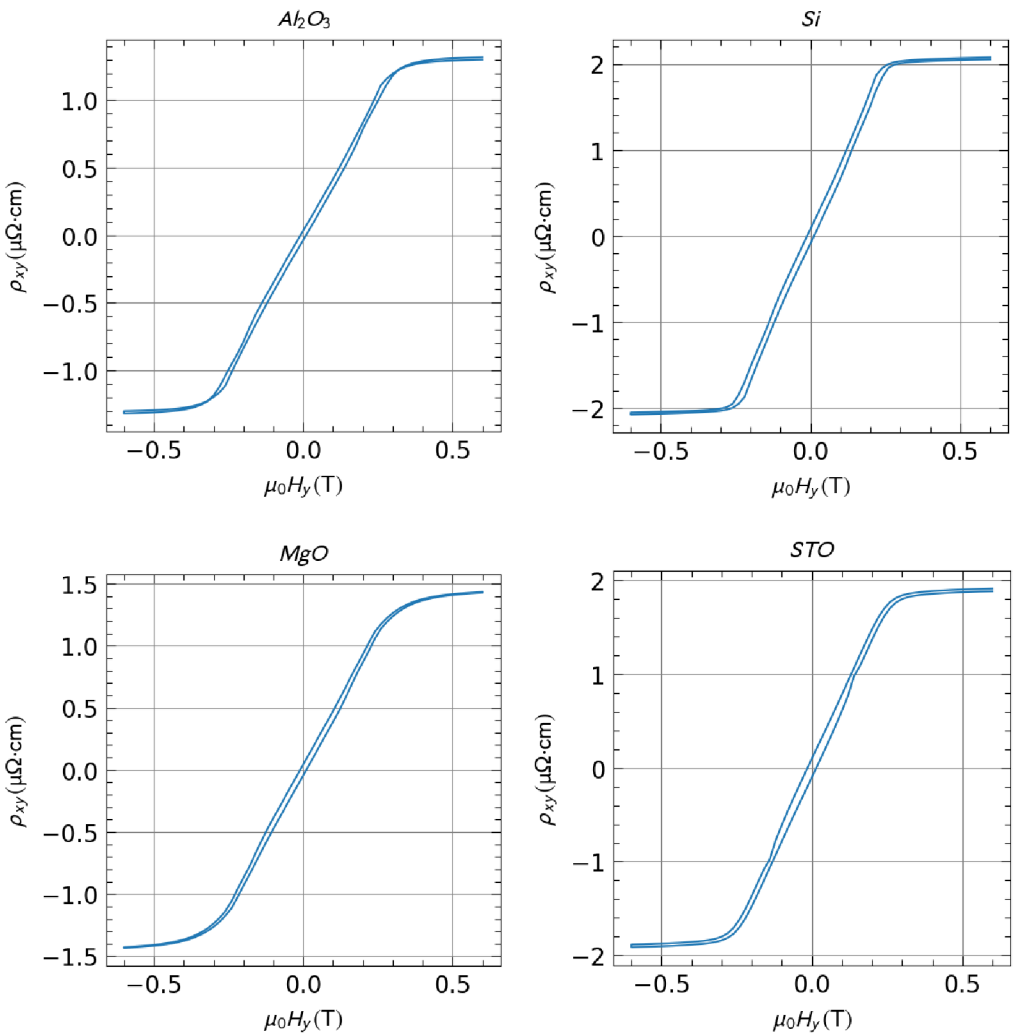


*Figure 30: Dependence of transverse resistivity in permalloy sample with different substrate materials on applied out-of-plane magnetic field.*

The measured field dependence of $\rho_{xy}$ is saturating around 0.3 T of the applied out-of-plane field. The saturation field agrees with the saturation field determined from the SQUID measurements in Figure 29. The saturating $\rho_{xy}$ signal in a ferromagnet is a characteristic sign of the anomalous Hall effect. The magnitude of the effect (i.e. the saturation value) is between 1.3 and 2.1 $\mu\Omega \cdot cm$.

There are multiple factors that may cause the variation of the AHE magnitude in our samples with different substrates. The substrate may influence the dynamics of permalloy crystal growth, and the grain size then can affect some of the magnetic properties of the material (62). Otherwise, an observed 30% difference in AHE magnitude may be due to the thickness difference of the sample. Profilometry results show the permalloy film thickness between 55 and 70 nm, which can depend on the location of the sample on the sample holder during the sputtering process. We use the averaged value of 60 nm to calculate the Hall effect magnitude.

## 4.2 Sample substrate influence on the ANE

We measured the influence of the substrate on the ANE measurements by conducting a series of experiments on the samples with the same geometry, at the same base temperature, and using the same heater power to exclude the influence of those factors on the measurement results.

As described before, we have used four different substrates: $Al_2O_3$ (0001), Si (100), $SrTiO_3$ (100), and MgO(100) single crystals. To generate temperature gradient in these samples, we used the configuration with macroscopic heaters illustrated in Figure 14.

The dependencies of the transverse thermoelectric signal on the magnitude of the applied magnetic field for the sample temperature of 150 K are shown in Figure 31. The signal shows saturation at about 0.3 T which complies with the saturation field observed in magnetization and AHE. The observed signal therefore corresponds to the anomalous Nernst effect. The magnitude of the signal varies between 0.18 µV/K on Si(111) substrate and 0.29 µV/K on the STO substrate.

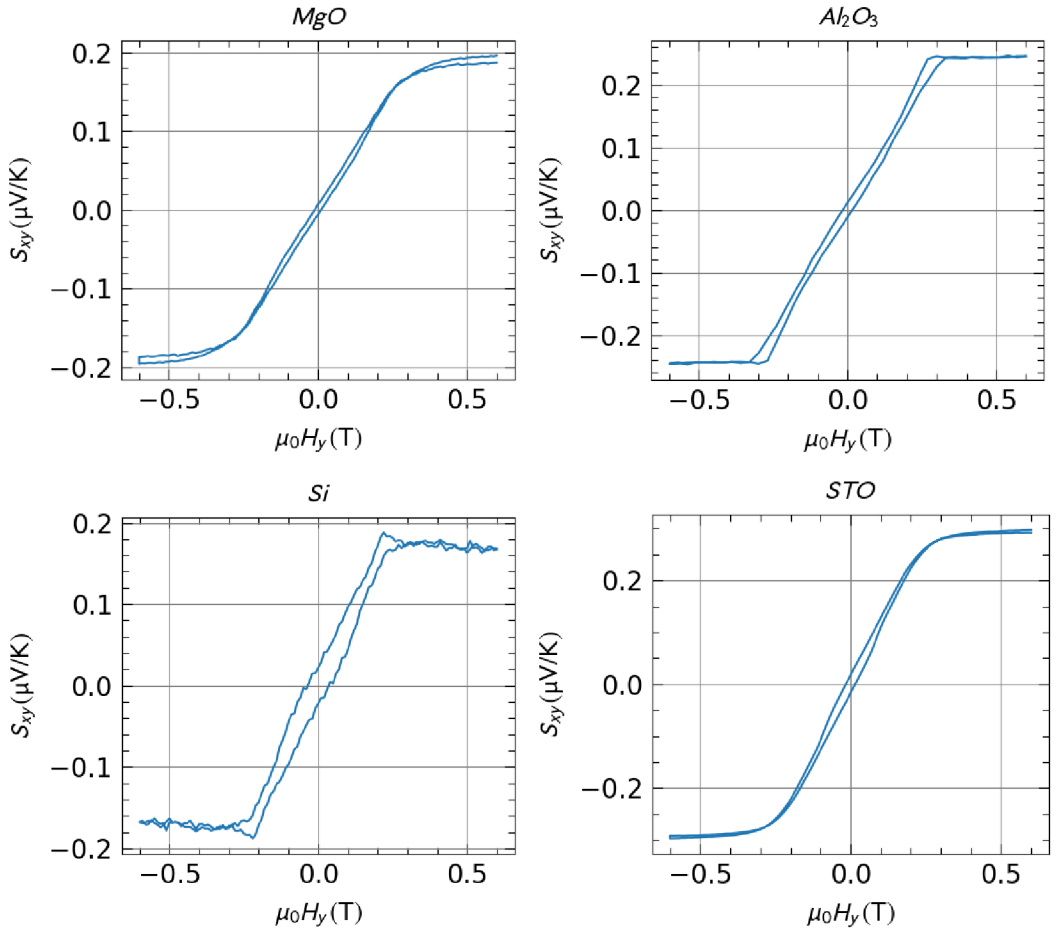


*Figure 31: Dependencies of the transverse thermoelectric signal on the magnitude of the applied magnetic field at 150 K*

Parameters of measurement, including achieved thermal gradient measured by the on-chip thermometers, calibrated sample temperature and heater power are shown in Table 1.

| Substrate\parameter | Thermal conductivity at 150 K, W/m·K | Temperature gradient, $K/mm$ | Sample temperature, $K$ | Heater power, $mW$ |
|---|---|---|---|---|
| $Al_2O_3$ | 449.8 | 2.976 | 177 | 623 |
| Si | 409 | 1.251 | 153 | 618 |
| STO | 20 | 13.200 | 149 | 627 |
| MgO | 114 | 4.759 | 149 | 632 |

*Table 1: Parameters of the ANE measurement on different substrates. (63) (64) (65) (66)*

As we can see from the measurement parameters, the achieved thermal gradient strongly correlates with the thermal conductivity of the substrate in Table 1. Differences in the sample temperature can be explained by slightly different helium pressure in the chamber, which depends on the liquid helium level in the cryostat. The temperature may have also been influenced by differently prepared interface between the sample and the heater or the heat sink, e.g. by a different amount of applied glue.

We also conducted finite-element simulations using COMSOL Multiphysics software. The comparison of the simulated and measured temperature gradients is shown in Table 2.

| Substrate | Measured gradient, K/mm | Simulated linearized gradient, K/mm |
|---|---|---|
| Si | 1.26 | 0.98 |
| $Al_2O_3$ | 2.98 | 0.87 |
| MgO | 4.76 | 3.30 |
| STO | 13.20 | 13.71 |

*Table 2: Comparison of the simulated and measured temperature gradients on the macroscopic heater configuration*

As we can see, the gradient values obtained from the simulations tend to underestimate temperature gradients on Si, $Al_2O_3$ and MgO substrates, while the simulated gradient value on STO is overestimated.

The difference in the magnitude of ANE signal on different substrates is higher than the difference in AHE magnitude. This proofs the crucial role of thermometer calibration for the ANE measurements.

## 4.3 Temperature gradient influence on the ANE

The sample on the STO substrate was tested using two settings of the heater power to determine the possible influence of the applied thermal gradient on the ANE signal. Using the script that controlled the current applied to the PT1000 resistor, the power of the heater was set to 627 mW in the first experiment and 446 mW in the second one. The base temperature of the cryostat was chosen such to reach the same sample temperatures in both configurations. The results of the experiment are shown in Figure 32.

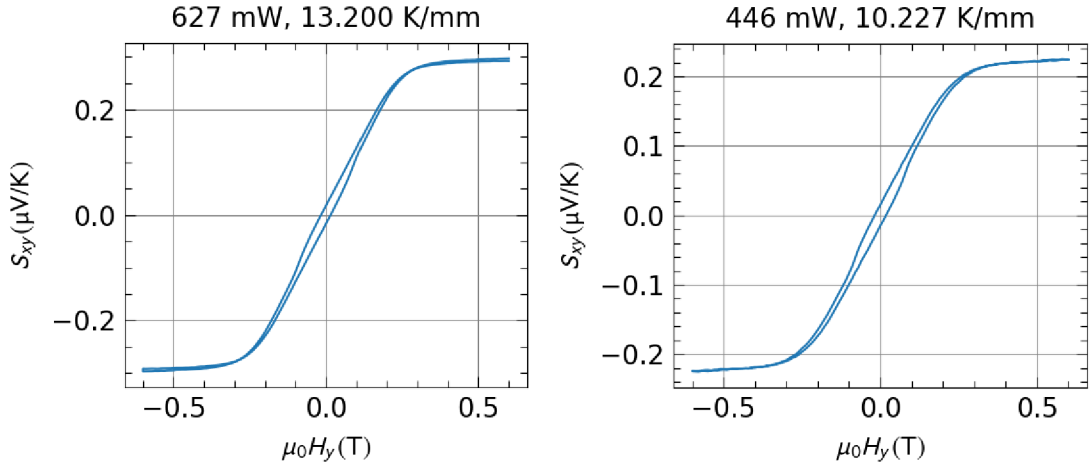


*Figure 32: Comparison of ANE signal for different temperature gradients*

Using two different power configurations, we achieved two different temperature gradient magnitudes, which were 13.200 K/mm and 10.227 K/mm respectively. Slight difference in the ANE magnitude, which is 0.29 $\mu V/K$ for 627 mW power and 0.22 $\mu V/K$ for 446 mW power can be considered a measurement error. However, the chosen method of temperature measurement and the calibration of the temperature gradient is robust with respect to the thermal gradient magnitude.

## 4.4 Temperature dependence of ANE at different temperatures

To determine the temperature effect on the ANE measurement we conducted a series of experiments on the same sample (STO substrate) at different sample temperatures of 100 K, 150 K, and 200 K. Results of those experiments are shown in Figure 33.

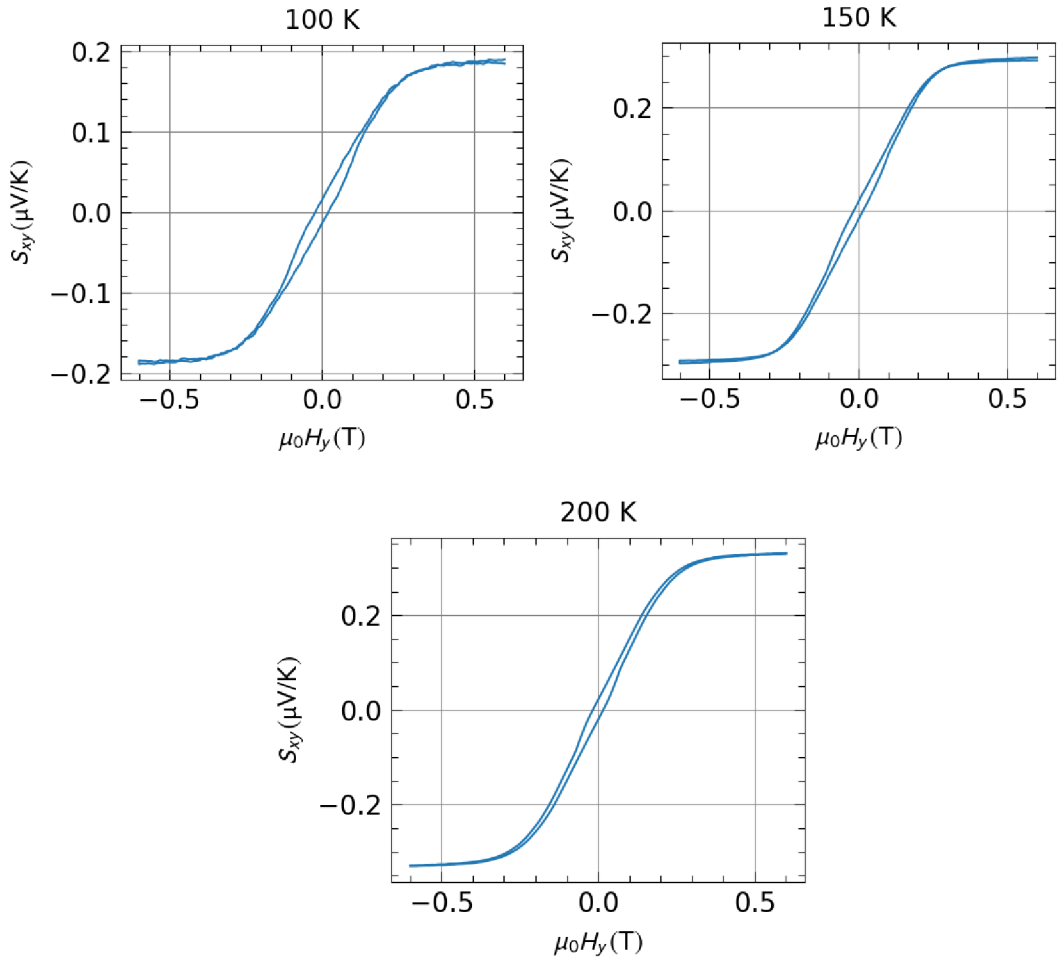


*Figure 33: Comparison of the ANE signal magnitude at different temperatures*

As we can see from the graphs of the transverse voltage dependence on the external magnetic field, the magnitude of ANE grows with increasing temperature from 0.19 $\mu V/K$ at 100 K to 0.33 $\mu V/K$ at 200 K, which was also observed for permalloy by other studies (67).

## 4.5 Measurement geometry influence of the ANE

Aside from the described macroscopic heater measurement configuration, we tested three other configurations of temperature gradient generation, which were previously used in different ANE research studies (see the introduction).

### 4.5.1 On-chip heater configuration

The widely used way to create a thermal gradient in the sample is using sputtered platinum stripes not only as thermometers, but as a Joule heating element too. In this configuration, current is applied to the platinum stripe located further from the center of the sample (see Figure 17), and the thermal gradient is measured using the stripes located closer to the center of the sample. The power of this type of heaters is limited due to possible meltdown at higher currents. However, we achieved the power of 300 mW creating a thermal gradient of 0.591 K/mm at 142 K on an $Al_2O_3$ substrate. The results of the experiment are shown in Figure 34.

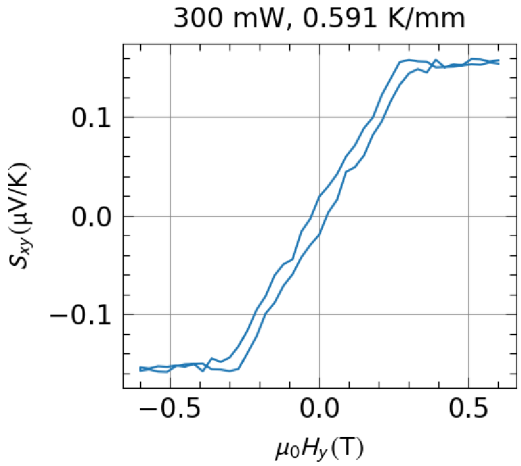


*Figure 34: ANE signal graph for on-chip heater configuration*

The magnitude of the ANE signal is 0.16 μV/K, which is comparable to experiments with the macroscopic heater geometry with the ANE magnitude of 0.25 μV/K, difference is caused by the different measurement base temperature, which was 177 K for measurement on the macroscopic heater configuration and 142 K for the on-chip heater configuration.

### 4.5.2 Out-of-plane configuration

The temperature gradient does not have to be applied in the sample plane, but can be also applied perpendicular to the sample surface. However, the measurement of the out-of-plane temperature gradient requires complex multilayer lithographic structures. Since our permalloy film is polycrystalline, we consider it to be isotropic, and, as a consequence, the saturation value of the ANE is isotropic as well. This enables us to estimate the thermal gradient using the magnitude of ANE signal obtained by experiments in other configurations. Raw ANE signal plot is shown in Figure 35.

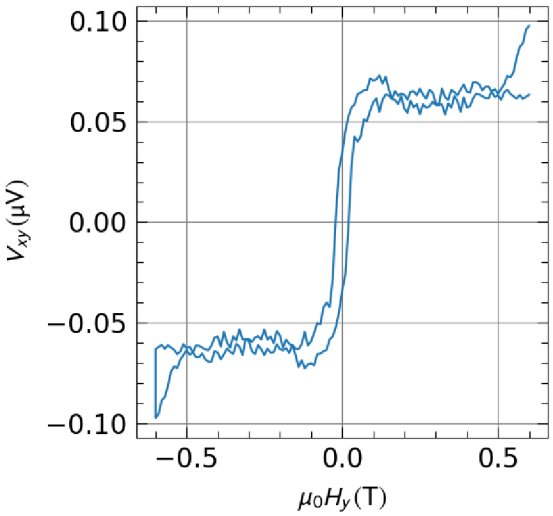


*Figure 35: Raw ANE signal for out-of-plane measurement configuration*

Using the magnitude of raw ANE signal at saturated field values ($|\mu_0 H_0| > 0.2\ T$) we can estimate the temperature gradient using the equation:

$$\nabla T = \frac{V_{xy}}{S_{xy} \cdot L}, \tag{4.1}$$

Where $V_{xy}$ is the raw ANE signal magnitude obtained from out-of-plane configuration, $S_{xy}$ is the ANE signal magnitude of the macroscopic heater sample on the same substrate ($Al_2O_3$), which is 0.24 μV/K, and L is the stripe length, which is 3 mm.

In this way, the thermal gradient was estimated to be 0.0893 K/mm. The generated temperature gradient is much smaller than in the other experimental configurations. However, this configuration enables us to probe the transport properties in the out-of-plane direction which may be often inaccessible by conventional electric transport, especially in single-crystal films.

### 4.5.3 Alternating gradient configuration

The main purpose of using a configuration with alternating temperature gradient is to minimize the influence of any unwanted factors on the magnitude of $S_{xy}$. To do so, we obtain 4 datapoints for each value of the field magnitude: two for the first heater with opposite current polarities, and two for the second heater with opposite current polarities. Using the delta-method, the acquired data was averaged, thus minimalizing errors arising due to any unwanted thermoelectrical factors. The acquired ANE signal plot is shown in Figure 36.

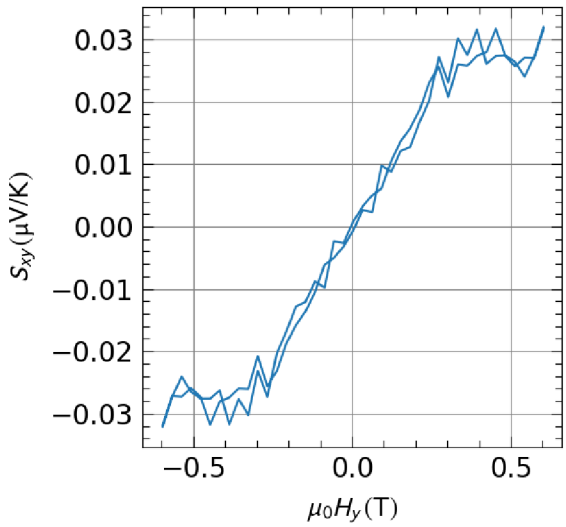


*Figure 36: ANE signal obtained from the alternating gradient configuration sample*

Unfortunately, the signal obtained from this sample is significantly lower than from the other samples on this substrate. This can be caused by failed thermometer calibration (PT100 thermometer was not functioning properly at the time of the measurement), or due to low heater power (geometry does not allow applying high current on the heater due to possible meltdown). However, we can see clear ANE pattern on the plot with coercive force close to zero, same as we have seen on the other samples.

## 4.6 Measurements on $Mn_5Si_3$

As it was mentioned in 2.3, the anomalous Nernst effect can also be present in materials with zero net magnetization, i.e. noncolinear antiferromagnets or altermagnets. Here, we applied the above-described techniques of the Nernst effect measurement on an altermagnetic material candidate $Mn_5Si_3$.

We use epitaxial layers of $Mn_5Si_3$ grown on intrinsic Si(111) with a MnSi buffer layer (68). The Nernst effect was measured in the configuration with macroscopic heaters with the heating power of 600 mW and the resulting temperature gradient of 1.6 K/mm. Figure 37 shows the field dependence of the $S_{xy}$ signal at the sample temperature of 81 K. The signal shows saturation at about 1.5 T and saturation magnitude of 0.1 μV/K.

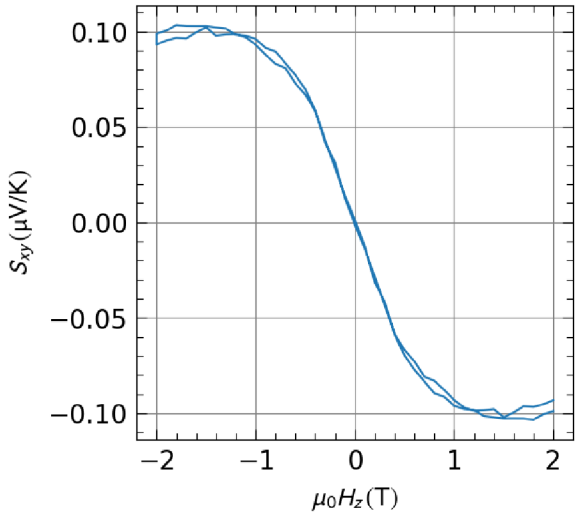


*Figure 37: Field dependence of the $S_{xy}$ signal on $Mn_5Si_3$ sample (T = 81 K)*

The observation of the anomalous Nernst effect in $Mn_5Si_3$ demonstrates that the finite Berry curvature arising from the anisotropically spin-split band structure of altermagnetic $Mn_5Si_3$ is reflected not only in the presence of the anomalous Hall effect (as shown by Reichlova et al. (31), but also by the finite anomalous Nernst effect.

# 5 Conclusion

This diploma thesis is dedicated to the systematic analysis of the role of substrate and experimental geometry in quantifying the anomalous Nernst effect in thin films. We investigated the influence of four different geometries and substrates. Permalloy, known for its pronounced anomalous Nernst effect, served as the reference material. We deposited Permalloy thin films on these substrates via magnetron sputtering under uniform conditions. The films' structures were characterized using X-ray diffraction and reflection techniques, while their magnetic properties were analyzed through SQUID magnetometry. Devices designed to study the anomalous Nernst effect were subsequently patterned using UV lithography. The samples displayed a clear anomalous Hall effect, with magnitudes ranging from 1.4 to 2 μΩ·cm, depending on the substrate.

The magnitude of the anomalous Nernst effect (ANE) was measured for each sample, ranging from 0.18 μV/K (on Si) to 0.29 μV/K (on STO), correlating with their thermal conductivity values. A critical factor in quantifying the ANE was the precise calibration of the thermal gradient, facilitated by lithographically defined on-chip thermometers and described details of this procedure.

We also compared various experimental geometries employing macroscopic and on-chip heaters. Results from both macroscopic and microscopic on-chip heater configurations were comparable, showing ANE coefficients of 0.16 and 0.29 μV/K, respectively. Differences in ANE coefficients can be attributed to varying base temperatures, confirmed by experiments conducted at different temperatures. Furthermore, the ANE magnitude increased with rising temperatures, as demonstrated by measuring the ANE on the STO substrate at three different base temperatures. Measuring the ANE at two different thermal gradient magnitudes confirms that our calibration of the temperature gradient is robust.

Careful quantification of the in-plane ANE magnitude was critical in estimating the temperature gradient in another geometry where the thermal gradient is applied in the out-of-plane direction. Although this geometry does not allow for direct measurements of the thermal gradient, the ANE magnitude enabled us to identify the out-of-plane thermal gradient as 0.0893 K/mm.

This thesis highlights the crucial role of precise thermal gradient calibration in determining the anomalous Nernst coefficient and outlines the optimal procedure for assessing the thermal gradient. In the final section, we apply this procedure to quantify the anomalous Nernst effect in an emerging compensated magnetic thin film, the altermagnetic candidate $Mn_5Si_3$, demonstrating a significant ANE value of 0.1 μV/K.

# References


1. **BLOCH, Felix.** Über die Quantenmechanik der Elektronen in Kristallgittern. *Zeitschrift für Physik.* 1929, 52(7)

2. **BLUNDELL, Stephen.** *Magnetism in condensed matter.* Oxford : OUP Oxford, 2001. 0198505914.

3. **KORUGA, D., et al.** Medical Devices Based on Mimicry in Light-Matter Interaction: "Structured Matter Meets Structured Light". [book auth.] S. Najman and et al. *Biomimetic and Other Compatible Materials Features for Medical Applications. Engineering Materials.* s.l. : Springer, Cham., 2023.

4. Magnetic domain. *wikipedia.org.* [Online] [Cited: April 19, 2023.] https://en.wikipedia.org/wiki/Magnetic_domain.

**5. NAGAOSA, Naoto, et al.** Anomalous Hall effect. *Rev. Mod. Phys.* 1539, 5 2010, 82(2).

**6. GÎRŢU, M. A., et al.** Coexistence of glassiness and canted antiferromagnetism in triangular quantum Heisenberg antiferromagnets with weak Dzyaloshinskii-Moriya interaction. *Phys. Rev. B.* 5 1998, 57(18).

**7. CHEN, Hua, NIU, Qian and MacDonald, A. H.** Anomalous Hall Effect Arising from Noncollinear Antiferromagnetism. *Phys. Rev. Lett.* 1 2014, 112(1)

**8. THOLAPI, Rajkiran.** Investigation of strained interfaces of Fe/(Ga, Al, In) As spintronic heterojunctions. 2018.

**9. TUREK, Ilja.** Altermagnetism and magnetic groups with pseudoscalar electron spin. *Phys. Rev. B.* 1 2022, 106.

**10. ŠMEJKAL, Libor, SINOVA, Jairo and JUNGWIRTH, Tomas.** Beyond Conventional Ferromagnetism and Antiferromagnetism: A Phase with Nonrelativistic Spin and Crystal Rotation Symmetry. *Phys. Rev. X.* 7 2022, 12(3).

**11. ŠMEJKAL, Libor, SINOVA, Jairo and JUNGWIRTH, Tomas.** Emerging Research Landscape of Altermagnetism. *Phys. Rev. X.* 10 2022, 12(4).

**12. MAZIN, Igor, et al.** Prediction of unconventional magnetism in doped FeSb2. *Proc. Natl. Acad. Sci. USA.* 2021, 118.

**13. DRUDE, P.** Zur Elektronentheorie der Metalle. *Ann. Phys.* 306, 1900, 566-613.

**14. LANDAU, Lev Davidovich, et al.** *Electrodynamics of continuous media.* s.l. : Elsevier, 1984. 978-0-08-030275-1.

**15. ASHCROFT, N. and MERMIN, K.** *Solid state physics.* New York : Holt-Saunders, 1976. 978-0030839931.

**16. GU, Hongbo, et al.** An overview of the magnetoresistance phenomenon in molecular systems. *Chemical society review.* 2013, 42(13).

17. Interview with the staff of Mizuguchi Lab (Nano-Spin and Magnetic Materials Development Engineering Group). *Institute of Materials and Systems for Sustainability.* [Online] 2021. [Cited: April 19, 2024.] https://www.imass.nagoya-u.ac.jp/en/interview_mizuguchi.

**18. BEHNIA, Kamran and AUBIN, Hervé.** Nernst effect in metals and superconductors: A review of concepts and experiments. *Reports on Progress in Physics.* 3 2016, 79(4).

**19. TAZLOR, James M., et al.** Anomalous and topological Hall effects in epitaxial thin films of the noncollinear antiferromagnet $Mn_3Sn$. *Phys. Rev. B.* 3 2020, 101(9).

**20. KARPLUS, Robert and LUTTINGER, J. M.** Hall Effect in Ferromagnetics. *Phys. Rev.* 9 1954, 95(5).

**21. KONDO, Jun.** Anomalous Hall Effect and Magnetoresistance of Ferromagnetic Metals. *Progress of Theoretical Physics.* 4 1962, 27(4).

**22.** Quantal phase factors accompanying adiabatic changes. *Proceedings of the Royal Society A Mathematical, Physical and Engineering Sciences.* Royal Society, 3 1984, 392(1802).

**23. SAKURAI, J. J. and NAPOLITANO, Jim.** *Modern Quantum Mechanics.* s.l. : Cambridge University Press, 2020. 9781108587280.

**24. DIEBOLD, A. and HOFMANN, T.** Hall Effect Characterization of the Electrical Properties of 2D and Topologically Protected Materials. *Optical and Electrical Properties of Nanoscale Materials. Springer Series in Materials Science, 318(1)* : Springer, Cham. , 2021.

**25. XIAO, Di, et al.** Berry-phase effect in anomalous thermoelectric transport. *Phys. Rev. Lett.* 2006, 97(2).

**26. IKEDA, Tomoki, et al.** Anomalous Hall effect in polycrystalline $Mn_3Sn$ thin films. *Appl. Phys. Lett.* 11 2018, 113(22).

**27. KIYOHARA, Naoki, TOMITA, Takahiro and NAKATSUJI, Satoru.** Giant Anomalous Hall Effect in the Chiral Antiferromagnet $Mn_3Ge$. *Phys. Rev. Applied.* 6 2016, 5(6).

**28. LIU, Z. H., et al.** Transition from Anomalous Hall Effect to Topological Hall Effect in Hexagonal Non-Collinear Magnet $Mn_3Ga$. *Scientific Reports.* 3 2017, 7(1)

**29. BECKERT, Sebastian, et al.** Anomalous Nernst effect in $Mn_3NiN$ thin films. *Phys. Rev. B.* 7 2023, 108(2)

**30. ŠMEJKAL, Libor, et al.** Crystal time-reversal symmetry breaking and spontaneous Hall effect in collinear antiferromagnets. *Science Advances.* 6 2020, 6(23).

**31. REICHLOVÁ, Helena, et al.** Macroscopic time reversal symmetry breaking arising from antiferromagnetic Zeeman effect. *arxiv: Mesoscale and Nanoscale Physics.* 2 2020, https://arxiv.org/abs/2012.15651v2.

**32. BRUNO, P., DUGAEV, V. K. and TAILLEFUMIER, M.** Topological Hall Effect and Berry Phase in Magnetic Nanostructures. *Phys. Rev. Lett.* 8 2004, 93(9)

**33. SURGERS, Christoph, et al.** Large topological Hall effect in the non-collinear phase of an antiferromagnet. *Nature Communications.* 3 2014, 5(1).

**34. YANAGIHARA, H. and SALAMON, M. B.** Skyrmion Strings and the Anomalous Hall Effect in $CrO_2$. *Phys. Rev. Lett.* 10 2002, 89(18).

**35. LEE, Wei-Li, et al.** Anomalous Hall Heat Current and Nernst Effect in the $CuCr_2Se_{4-x}Br_x$ ferromagnet. *Phys. Rev. Lett.* 11 2004, 93(22).

**36. PU, Yong, et al.** Mott Relation for Anomalous Hall and Nernst Effects in $Ga_{1-x}Mn_xAs$ Ferromagnetic Semiconductors. *Phys. Rev. Lett.* 9 2008, 101(11)

**37. RAMOS, R., et al.** Anomalous Nernst effect of $Fe_3O_4$ single crystal. *Phys. Rev. B.* 8 2014, 90(5)

**38. MIZUGUCHI, Masaki, et al.** Anomalous Nernst Effect in an $L1_0$-Ordered Epitaxial FePt Thin Film. *Applied Physics Express.* The Japan Society of Applied Physics, 8 2012, 5(9)

**39. HASEGAWA, K., et al.** Material dependence of anomalous Nernst effect in perpendicularly magnetized ordered-alloy thin films. *Applied Physics Letters.* 6 2015, 106(25).

**40. SAKAI, Akito, et al.** Iron-based binary ferromagnets for transverse thermoelectric conversion. *Nature.* 5 2020, 581(7806)

**41. LI, Minghang, et al.** Large Anomalous Nernst Effects at Room Temperature in $Fe_3Pt$ Thin Films. *Advanced Materials.* 8 2023, 35(32).

**42. XU, Jinsong, PHELAN, W. Adam and CHIEN, Chia-Ling.** Large Anomalous Nernst Effect in a van der Waals Ferromagnet $Fe_3GeTe$. *Nano Lett.* 11 2019, 19(11).

**43. SCHEFFLER, D., et al.** Anomalous Nernst effect in perpendicularly magnetized τ-MnAl thin films. *AIP Advances.* 12 2023, 13(12).

**44. HE, Bin, et al.** Large magnon-induced anomalous Nernst conductivity in single-crystal MnBi. *Joule.* 11 2021, 5(11).

**45. GUIN, Satya N., et al.** Zero-Field Nernst Effect in a Ferromagnetic Kagome-Lattice Weyl-Semimetal $Co_3Sn_2S_2$. *Advanced Materials.* 6 2019, 31(25).

**46. ASABA, T., et al.** Colossal anomalous Nernst effect in a correlated noncentrosymmetric kagome ferromagnet. *Science Advances.* 3 2021, 7(13).

**47. LI, Xiaokang, et al.** Anomalous Nernst and Righi-Leduc Effects in $Mn_3Sn$. *Phys. Rev. Lett.* 8 2017, 119(5).

**48. IKHLAS, Muhammad, et al.** Large anomalous Nernst effect at room temperature in a chiral antiferromagnet. *Nature Physics.* 11 2017, 13(11).

**49. WUTTKE, Christoph, et al.** Berry curvature unravelled by the anomalous Nernst effect in $Mn_3Ge$. *Phys. Rev. B.* 8 2019, 100(8).

**50. HONG, Deshun, et al.** Large anomalous Nernst and inverse spin-Hall effects in epitaxial thin films of kagome semimetal $Mn_3Ge$. *Phys. Rev. Materials.* 9 2020, 4(9).

**51. NARITA, Hideki, et al.** Anomalous Nernst effect in a microfabricated thermoelectric element made of chiral antiferromagnet $Mn_3Sn$. *Applied Physics Letters.* 11 2017, 111(20).

**52. PAN, Yu, et al.** Giant anomalous Nernst signal in the antiferromagnet $YbMnBi_2$. *Nature Materials.* 2 2022, 21(2).

**53. XU, Chunqiang, et al.** Large anomalous Nernst effect and topological Nernst effect in the noncollinear antiferromagnet $NdMn_2Ge$. *Phys. Rev. B.* 8 2023, 108(6)

**54. REICHLOVÁ, Helena, SCHLITZ, Richard, et al.** Large anomalous Nernst effect in thin films of the Weyl semimetal $Co_2MnGa$. *Appl. Phys. Lett.* 2018, 113(21)

**55. WU, Stephen M., et al.** Spin Seebeck devices using local on-chip heating. *J. Appl. Phys.*, 2015, 117(17).

**56. BUDAI, Nico, et al.** High-resolution magnetic imaging by mapping the locally induced anomalous Nernst effect using atomic force microscopy. *Applied Physics Letters.* 2023, 122(3).

**57. BARTELL, J., NGAI, D., LENG, Z. et al.** Towards a table-top microscope for nanoscale magnetic imaging using picosecond thermal gradients. *Nat. Commun.* 2015, 6.

**58. BAĎURA, Antonin, et al.** Even-in-magnetic-field part of transverse resistivity as a probe of magnetic order. *arxiv: Condensed Matter, Mesoscale and Nanoscale Physics.* 2023, https://arxiv.org/abs/2311.14498v1.

**59. SCHLITZ, Richard., et al.** All Electrical Access to Topological Transport Features in $Mn_{1.8}PtSn$ Films. *Nano Lett.* 2019, 4.

**60.** MPMS XL 7T magnetometer. *mgml.eu.* [Online] [Cited: April 15, 2024.] https://mgml.eu/laboratories/instruments/mpms7.

**61. FERRERO, Riccardo, et al.** Influence of shape, size and magnetostatic interactions on the hyperthermia properties of permalloy nanostructures. *Scientific Reports.* 2019, 2.

**62. DJUZHEV, Nikolay, et al.** Effects of average grain size on the magnetic properties of permalloy films. *EPJ Web of Conferences.* 2018, 185(3).

**63.** Silicon. *Efunda, engineering fundamentals.* [Online] [Cited: April 10, 2024.] https://www.efunda.com/materials/elements/TC_Table.cfm?Element_ID=Si.

**64.** Corundum, Aluminum Oxide, Alumina, 99.9%, $Al_2O_3$. *MatWeb.* [Online] [Cited: April 10, 2024.] https://www.matweb.com/search/DataSheet.aspx?MatGUID=c8c56ad547ae4cfabad15977bfb537f1&ckck=1.

**65. SHELUDYAK, Yu. E., et al.** *Thermal Properties of Components of Combustible Systems [in Russian].* Moscow : s.n., 1982.

**66. MARTELLI, V., et al.** Thermal Transport and Phonon Hydrodynamics in Strontium Titanate. *Physical Review Letters.* 2018.

**67. BENNET, R. K., HOJEM, A. and ZINK, B.L.** Temperature dependence of the anomalous Nernst coefficient for $Ni_{80}Fe_{20}$ determined by metallic nonlocal spin valves. *AIP Advances.* 2020, 10

**68. KOUNTA, Ismaïla, et al.** Competitive actions of MnSi in the epitaxial growth of $Mn_5Si_3$ thin films on Si(111). *Phys. Rev. Materials.* 2023, 7(2)

**69. BAĎURA, Antonin.** *Magnetooptical and magnetotransport effects in non-collinear antiferromagnets.* Praha : UK, 2022. https://dspace.cuni.cz/handle/20.500.11956/174038.

**70. WENG, Hongming, et al.** Quantum anomalous Hall effect and related topological electronic states. *Advances in Physics.* 5 2015, 64(3).

**71. GOMONAJ, E. V.** Magnetostriction and piezomagnetism of noncollinear antiferromagnet $Mn_3NiN$. *Phase Transitions.* 7 1989, Vol. 18, 1-2, pp. 93-101.

**72. HAMOUDA, Samir.** *Physics Department Solid State Physics Graduate Level / Course 4533.* 2024.

**73. RUIHAO, Liu, et al.** Anomalous Nernst effect in compensated ferrimagnetic $Co_xGd_{1-x}$ films. *Applied Physics Letters.* 122, 2023, Vol. 2.

**74. WU, Y., et al.** AC measurement of the Nernst effect of thin films at low temperatures. *Rev. Sci. Instrum.* 2020, 91(9).

**75. YAMAZAKI, Takumi, et al.** Thickness dependence of anomalous Hall and Nernst effects in Ni-Fe thin films. *Physical review B.* 2022, 105.

# List of Abbreviations

AFM – atomic force microscopy
AHE – the anomalous Hall effect
ANE – the anomalous Nernst effect
OMR – ordinary magnetoresistance
PCB – printed circuit block
PLA – polylactic acid
SQUID – superconducting quantum interference device
STO – $SrTiO_3$, strontium titanate
VTI – variable temperature insert
XRD – x-ray diffraction (technique)
XRR – x-ray reflection (technique)